# Mitigating the damage of ultra-high performance concrete at elevated temperatures using synergistic flame-retardant polymer fibres

Tong Zhang[a,b], Mingzhong Zhang[b], Yi Shen[a], Hehua Zhu[a], Zhiguo Yan[a,*]

[a] State Key Laboratory of Disaster Reduction in Civil Engineering, College of Civil Engineering, Tongji University, Shanghai 200092, China

[b] Department of Civil, Environmental and Geomatic Engineering, University College London, London WC1E 6BT, UK

**Abstract:** Ultra-high performance concrete (UHPC) is vulnerable to high temperature-induced damage due to its dense microstructure. To mitigate thermal damage of UHPC, this study develops synergistic flame-retardant polymer (SFRP) fibres by introducing organic-metallic fillers and experimentally investigates the thermal properties, compressive behaviour, and microstructural evolution of SFRP fibre reinforced UHPC subjected to elevated temperatures up to 800 °C. Results indicated that the addition of SFRP fibres can effectively prevent the explosive spalling and significantly reduce the strength loss of UHPC at high temperatures due to the thermal mismatch between fibres and concrete. SFRP fibres were also proved to help greatly enhance the fire resistance and mitigate the thermal damage of UHPC, which can be attributed to the increased connectivity of pore structure, filling effect of flame-retardant polymers, and delayed degradation of micromechanical properties. The SFRP fibre content of 2.0 vol% is recommended considering the residual strength and damage mitigation efficiency.

*Keywords:* Ultra-high performance cementitious composites; Fibre reinforced concrete; Damage evolution; Fire resistance; Pore structure

## 1. Introduction

Because of the low water-to-binder (w/b) ratio, ultra-high performance concrete (UHPC) possesses dense microstructure with greatly reduced porosity and permeability, leading to high compressive strength and superior toughness and durability [1,2]. However, the dense microstructure also makes UHPC highly vulnerable to damage induced by high temperatures [3,4]. Concrete would experience complex hydraulic and chemical processes when subjected to elevated temperatures, such as loss of moisture content, decomposition of hydration products and deterioration of limestone aggregates [5,6]. The thermal damage of concrete, especially the explosive spalling, is a primary concern for design and maintenance of concrete infrastructures, which can pose a great threat to both human evacuation and structural safety [7–9]. The thermal damage of UHPC can be attributed to the combined effects of (i) the build-up pore pressure due to water evaporation [10]; (ii) the thermal stresses induced by temperature gradients [11]; and (iii) the degradation of micromechanical properties due to decomposition of hydration products [12,13]. The former two aspects would cause tensile stress and micro-cracking in UHPC matrix, while the over-saturated vapour hindered in the pore structure of UHPC could trigger violent spalling of concrete blocks [14]. Moreover, the

temperature-dependent elastic modulus and instantaneous phase composition of hydration products including calcium silicate hydrates (C–S–H), calcium hydroxide (CH), and aluminate hydrates would directly lead to the reduction in mechanical properties of UHPC [15,16]. Therefore, it is vital to find effective methods to avoid or mitigate thermal damage and explosive spalling, as well as improve the mechanical and thermal properties of UHPC at elevated temperatures.

Over the past decades, many attempts have been made to enhance the fire resistance of UHPC, and increased attention has been paid to the addition of hybrid micro- and meso-size particulate or fibrous inclusions. For instance, fly ash cenospheres and glass microspheres were used as typical particulate fillers to develop ultra-lightweight cementitious composites with high specific strength [17–19]. Micro-encapsulated phase change materials were utilised to promote the thermal mass effect, heal the thermally induced cracks and thereby reduce the energy consumption of concrete [20,21]. However, these meso-size particles may be insufficient to mitigate the damage of concrete subjected to high temperatures, and only with the help of fibrous inclusions, e.g. a combination of fly ash cenospheres and polypropylene (PP) fibres, can effectively eliminate the explosive spalling of concrete at up to 900 $^{o}$C [22]. Hybrid steel, polymer, and natural fibres were found to be more effective in enhancing the fire resistance of UHPC. The addition of steel fibres alone has negligible contribution to the resistance of UHPC from explosive spalling [23]. As revealed by X-ray computed tomography, the presence of steel fibres decreases the initial porosity of UHPC but leads to a more significant loss of strength induced by high-temperature thermal damage [24]. In contrast, polymer fibres such as PP, polyamide 66, low-density polyethene, and polyvinyl alcohol (PVA) fibres were found to be effective in preventing explosive spalling of UHPC at high temperatures [3,25–27]. The primary mechanism for spalling inhibition is the increased permeability due to phase changes (i.e., melting and vaporization) of polymer fibres [10], as well as the expansion of interfacial transition zone (ITZ) between fibre and cement paste [28]. It is noted that there exists a thermal mismatch between PP fibres and UHPC matrix, and the thermal expansion coefficient of PP is 10 times greater than that of cement paste at 140 $^{o}$C [29]. As a result, micro-cracks generated by fibre expansion would cause the increase in permeability of UHPC matrix even before the melting of polymer fibres [25]. Similarly, the incompatibility between steel fibres and cement paste can also induce micro-cracks along the radial direction of embedded steel fibres, and accordingly the synergistic effects of hybrid PP and steel fibres would significantly increase the permeability of UHPC matrix at low fibre dosages [23]. In addition, the combined usage of two types of steel fibres (with different lengths of 13 and 30 mm) and PP fibres (with length of 24 mm) can prevent spalling and preserve the compressive strength of UHPC even after long-term heating at moderate temperatures (up to 300 $^{o}$C) for 24 h [30]. Apart from the manufactured fibres, natural jute fibre was also proved to help inhibit explosive spalling, which can be ascribed to the additional gaps between jute fibres and UHPC matrix resulted from deswelling and shrinkage of natural fibres [31]. A

dosage of 10 kg/m$^3$ of jute fibres was suggested to completely eliminate spalling in comparison with only 4 kg/m$^3$ of PP fibres [32]. However, the above-mentioned fibrous inclusions would have negative effects on the mechanical properties of UHPC due to their relatively low elastic modulus and bending stiffness, and the negative effect may be more obvious at elevated temperatures [4–6]. Overall, there is still lack of an effective method to improve the fire resistance of UHPC without compromising other mechanical properties [4].

In the previous study [33], a novel type of synergistic flame-retardant polymer (SFRP) fibre composed of intumescent flame retardants and polymer resin was fabricated to enhance the fire resistance of concrete, while it has a negative effect on the mechanical properties of concrete. The main purpose of this study is to develop a more effective type of SFRP fibre by introducing organic-metallic fillers to mitigate the damage evolution of UHPC at elevated temperatures but not impair its mechanical properties. A series of tests were conducted to systematically estimate the effects of type and volume fraction of SFRP fibres on the mechanical and thermal properties of UHPC subjected to elevated temperatures up to 800 $^o$C in terms of mass loss, compressive properties, thermal conductivity and temperature distribution. The chemical and micromechanical properties of SFRP fibres were characterised using X-ray diffraction (XRD), Fourier transform infrared (FTIR) spectroscopy, microscale combustion calorimetry (MCC), thermo-gravimetric (TGA), differential scanning calorimetry (DSC), and atomic force microscopy (AFM). The evolution of microstructure and micromechanical properties of SFRP fibre reinforced UHPC were explored using confocal laser scanning microscopy (CLSM), electron probe micro analysis (EPMA), mercury intrusion porosimetry (MIP), and nanoindentation. Based on the obtained microscopic and macroscopic results, the efficiency of SFRP fibres in mitigating thermal damage of UHPC at elevated temperatures and the underlying mechanisms were discussed in depth.

## 2. Experimental program

### 2.1. Raw materials

In this study, granular polypropylene (PP) was used as the polymer resin matrix to produce SFRP fibres. The density and melting temperature of PP particles are 0.90 g/cm$^3$ and 159 $^o$C, respectively. The organic intumescent flame retardants were composed of ammonium polyphosphate (APP), melamine (MEL), and pentaerythritol (PER). To improve the mechanical and thermal properties of flame-retardant fibres, $Mg(OH)_2$ and $Al(OH)_3$ powder was incorporated as the metallic fillers. Besides, stearic acid (SA) was added as a safe and non-toxic lubricant agent. All these chemicals for SFRP fibres are commercially available.

P.I 52.5R ordinary Poland cement, silica fume, fly ash, water, and fine bauxite aggregate were used to produce UHPC matrix. The special surface area of silica fume and fly ash is 26 and 20 m$^2$/g, respectively. The main content of fine aggregate is $Al_2O_3$ (alumina, over 60% by mass), the particle size of which ranges from 0.12 to 0.83 mm. Polycarboxylate superplasticizer (SP, Melment F10,

BASF) with a 1.5 wt.% dosage of cement was added to enhance the workability of UHPC. The chemical compositions of these raw materials are presented in Table 1.

**Table 1** Chemical compositions (wt.%) of cement and admixture blinders.

| Type | $SiO_2$ | CaO | MgO | $Al_2O_3$ | $Fe_2O_3$ | $Na_2O$ | Others |
|---|---|---|---|---|---|---|---|
| Cement | 20.84 | 65.73 | 3.08 | 5.21 | 3.25 | 0.96 | 0.93 |
| Silica fume | 93.76 | 1.28 | 1.19 | 0.64 | 0.87 | 0.98 | 1.28 |
| Fly ash | 61.45 | 1.64 | 1.07 | 28.13 | 4.92 | 1.25 | 1.54 |

### 2.2. Mix proportions and sample preparation

2.2.1. Fabrication of synergistic flame-retardant polymer fibres

In this study, two types of synergistic flame-retardant polymer fibres were fabricated, namely organic polymer (OP) and modified polymer (MP) fibres. As per the previous studies [33–35], the mass ratio of organic flame retardants APP-MEL-PER was set as 2:2:1 in both types of SFRP fibres. For MP fibre only, one-third mass fraction of the organic retardants was replaced by metallic intumescent retardants $Mg(OH)_2$ and $Al(OH)_3$ with a mass ratio of 2:1 [36]. The chemical proportions of two types of SFRP fibres are given in Table 2.

The synergistic flame-retardant polymer fibres were fabricated by means of melt extrusion and cooling moulding methods, as illustrated in Fig. 1. Firstly, the raw materials in the form of solid were weighed and dry-mixed for 10 min. Then, the mixture was poured into the feeding port, after which the mixture was transformed into the heaters using the twin screws. The melt compounding and extrusion of the composite materials were conducted using a co-rotating twin-screw extruder (Hartek, HTGD-20, China) with the temperature of different heaters between 165 and 180 ℃. Finally, the extruded needle-like composites were cooling moulded in the water sink and cut into suitable length through a pelletizer machine. The average diameter and length of the obtained flame-retardant polymer fibres were 0.5 mm and 10.0 mm, respectively. Table 3 summarises the physical and mechanical properties of fabricated SFRP fibres.

**Table 2** Chemical compositions (wt.%) of synergistic flame-retardant polymer fibres.

| Fibre type | PP resin matrix | Organic intumescent flame retardants | | | Metallic fillers | | SA |
|---|---|---|---|---|---|---|---|
| | | APP | MEL | PER | $Mg(OH)_2$ | $Al(OH)_3$ | |
| OP | 50.0 | 16.0 | 16.0 | 8.0 | – | – | 10.0 |
| MP | 50.0 | 10.7 | 10.7 | 5.3 | 8.9 | 4.4 | 10.0 |

Note: OP – organic polymer fibre, MP – modified polymer fibre, APP – ammonium polyphosphate, MEL – melamine, PER – pentaerythritol, SA – stearic acid.

**Table 3** Physical and mechanical properties of synthetic flame-retardant fibres.

| Fibre type | Length (mm) | Diameter (mm) | Density ($g/cm^3$) | Elongation (%) | Tensile strength (MPa) | Elastic modulus (MPa) |
|---|---|---|---|---|---|---|
| OP | 10.0 | 0.5 | 1.28 | 22 | >850 | >7000 |
| MP | 10.0 | 0.5 | 1.41 | 15 | >1460 | >12000 |

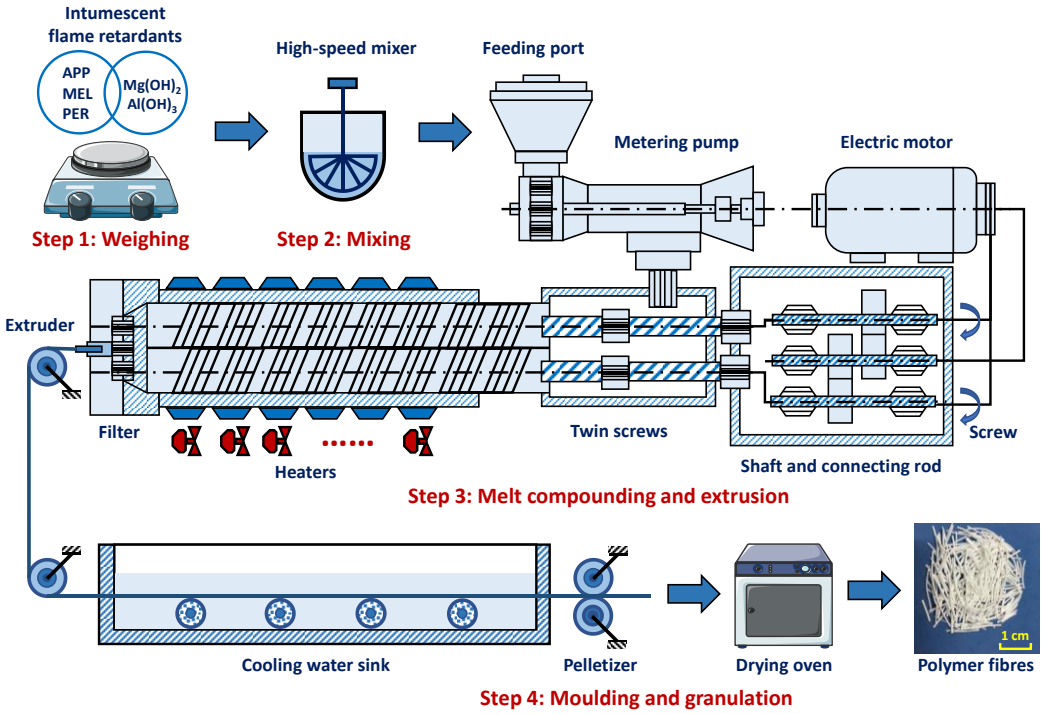


**Fig. 1.** Illustration of the fabrication processes of synthetic flame-retardant polymer fibres through melting extrusion and cooling moulding.

2.2.2. Preparation of synthetic flame-retardant polymer fibre reinforced UHPC

For plain UHPC mix, the w/b ratio of 0.20 was adopted to obtain appropriate workability of mixture [3,25]. OP and MP fibres were separately incorporated into UHPC with volume fractions of 1.0% and 2.0%, so four mixtures of fibre reinforced UHPC (FRC) in total were considered in this study. As reported in [27,37], the addition of polymer fibres with over 2.0 vol% can lead to up to 25% loss of compressive strength. Therefore, 2.0% was selected as the maximum SFRP fibre content to avoid too much strength loss, as well as 1.0% to investigate the effect of fibre content on thermal damage of UHPC. The mix proportions of UHPC specimens are listed in Table 4. The mixing process of UHPC was kept consistent with that presented in previous studies [23,38]. Firstly, the cement, fly ash, silica fume and fine aggregates were dry-mixed in a planetary-type concrete mixer for 2 min. Afterwards, the premixed water and superplasticizer were added into solid ingredients and mixed for another 3–5 min until the fresh concrete matrix was consistent and homogenous. Then, SFRP fibres were gradually added in 3–5 min and mixed for another 2 min to ensure the uniform dispersion of fibres. In what follows, fresh UHPC mixture was poured into oiled plastic moulds with sizes of 100×100×100 and 400×400×60 $mm^3$, to make specimens for the compression test, thermal conductivity test and one-side heating test. Part of the cubic specimens with the side length of 100 mm were cut into two identical pieces for further measurement of thermal conductivity. Table 5 provides more details about the dimension, number, and test condition of each UHPC specimen. In additional, K-type thermocouples with different embedded lengths were fitted to the moulds with the size of 400×400×60 $mm^3$. The reserved thermocouples were used to measure the

temperature distribution of UHPC slabs during the one-side heating test [39]. After casting, all UHPC specimens were covered with plastic films and kept under a standard condition (20±2 °C, 95% relative humidity) for 24 h, which were then demoulded and cured under water for 27 d.

**Table 4** Mix proportions of plain UHPC and FRC specimens.

| Mix ID | Mix proportions of UHPC matrix (kg/m$^3$) | | | | | | Fibre content (vol%) | |
|---|---|---|---|---|---|---|---|---|
| | Cement | Water | Aggregate | Silica fume | Fly ash | PBS | OP | MP |
| Plain UHPC | 745.9 | 233.1 | 1025.6 | 233.1 | 186.5 | 11.2 | – | – |
| FRC-OP01 | 745.9 | 233.1 | 1025.6 | 233.1 | 186.5 | 11.2 | 1.0 | – |
| FRC-OP02 | 745.9 | 233.1 | 1025.6 | 233.1 | 186.5 | 11.2 | 2.0 | – |
| FRC-MP01 | 745.9 | 233.1 | 1025.6 | 233.1 | 186.5 | 11.2 | – | 1.0 |
| FRC-MP02 | 745.9 | 233.1 | 1025.6 | 233.1 | 186.5 | 11.2 | – | 2.0 |

Note: PBS–polycarboxylate superplasticizer.

**Table 5** Details of the thermal and mechanical tests of UHPC at elevated temperatures.

| Test | Specimen size (mm$^3$) | Specimen number | Test temperature (°C) |
|---|---|---|---|
| Compressive strength test | 100×100×100 | 5 (M)×5 (T)×3 (R) | 20, 200, 400, 600, 800 |
| One-side heating test | 400×400×60 | 5 (M) | ISO 834 curve [40] |
| Thermal conductivity test | 100×100×50 | 3 (M)×5 (T)×2 (P) | 20, 200, 400, 600, 800 |

Note: M – mixture, T – temperature, R – replication, P – piece; the thermal conductivity test was conducted on plain UHPC and FRC mixtures with 2 vol% OP/MP fibre.

### 2.3. Characterisation of synthetic flame-retardant polymer fibres

#### 2.3.1. X-ray diffraction

The crystal structure of SFRP fibres was measured using a XPert diffractometer (PANalytical, PRO, Netherlands) operating at an accelerating voltage of 40 kV. Under continuous scanning pattern, Cu Kα radiation worked as the source of X-rays with a wavelength of 0.1541 nm, and crystalline phases were scanned from10° to 80° with a 2$\theta$ increment of 0.02 °/step.

#### 2.3.2. Fourier transform infrared spectroscopy

To characterise the chenical reactions, SFRP fibres in the form of powder were sampled with KBr powder at the mass ratio of 1:100. Fourier infrared spectra of samples were recorded using an infrared spectrometer (Thermo Fisher, Nicolet 5700, USA) over the wavenumber range of 4000–400 cm$^{-1}$. FTIR sans were conducted at both ambient temperature and elevated temperatures.

#### 2.3.3. Microscale combustion calorimetry

The flammability characteristics of SFRP fibres were measured through combustion calorimetry, operating at a microscale combustion calorimeter (Deatak, PCFC, USA). According to ASTM D7309 [41], the flow rate between $N_2$ and $O_2$ was set as 4:1 to simulate the air atmosphere, and the combustor temperature was set as 900 °C with a heating rate of around 1 °C /s.

#### 2.3.4. Thermo-gravimetric and differential scanning calorimetry

The thermal properties of SFRP fibres were analysed through TG-DSC coupled measurements using a thermal analyser (NETZSCH, STA 449C, Germany). The samples were dried in a vacuum

oven until a constant mass was obtained. Then, accurately weighted (about 5 mg) samples were heated under continuous $N_2$ atmosphere from 20 to 1000 $^oC$ with a heating rate of 10 $^oC$ /min.

2.3.5. Atomic force microscopy

By monitoring the Van der Waal force of silicon nitride ($Si_3N_4$) probes, the local adhesion and elastic modulus of SFRP fibres were measured simultaneously using an atomic force microscope (Park, NX-Hivac, Korea). The observation area was 5×5 $\mu m^2$, and the default frequency was 2 kHz under the peak-force tapping mode.

**2.4. Characterisation of synthetic flame-retardant polymer fibre reinforced UHPC**

2.4.1. Compression test

The residual compressive strength of UHPC after heat exposure was evaluated by uniaxial compression test. Firstly, cubic UHPC specimens were exposed to elevated temperatures in a muffle furnace. The temperature of furnace was increased from ambient temperature to target temperatures with a constant heating rate of 5 $^oC$ /min and maintained at the maximum temperature for 2 h to ensure the whole specimen reaches the target temperature [42]. Then, UHPC specimens were naturally cooling down to ambient temperature in the furnace, and the mass of specimens before and after heat exposure was weighted and recorded. Fig. 2a shows the heating and cooling curves of the furnace. Afterwards, compressive strength tests were performed using an electro-hydraulic servo testing machine (WANCE, HUT305D, China) with a maximum capacity of 3000 kN. The force loading mode was adopted for measuring the compressive strength with a loading rate of 0.20 MPa/s according to GB/T 50081 [43]. In total, five temperature levels were considered in compressive strength tests, including 20, 200, 400, 600 and 800 $^oC$. To ensure the reliability of results, three UHPC specimens with the same mix proportion at each temperature level were tested.

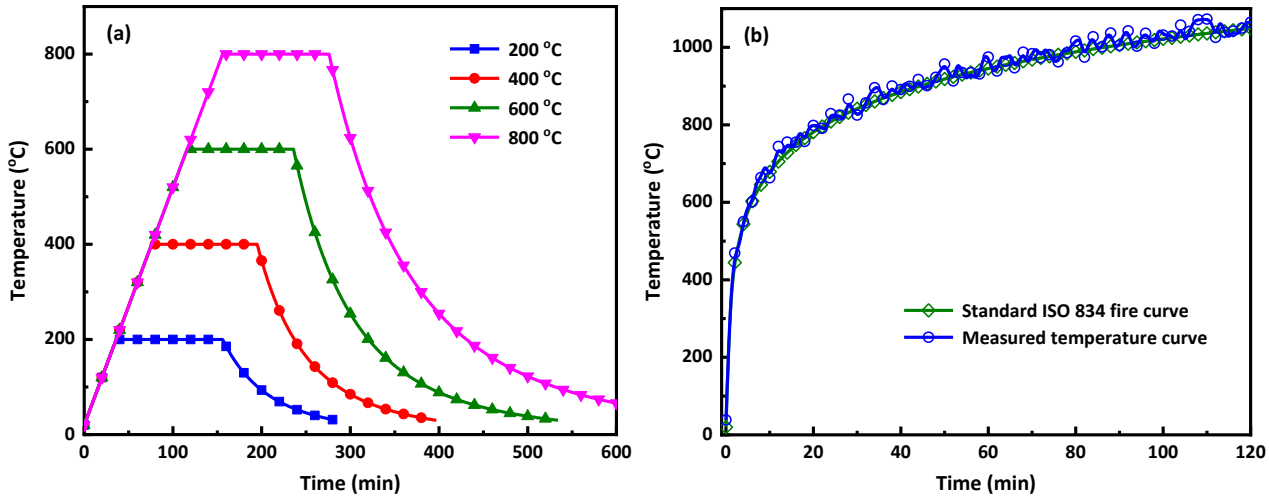


**Fig. 2.** Temperature curves for (a) compressive strength test, and (b) one-side heating test.

2.4.2. One-side heating test

The event of a fire usually just affects one side of the concrete structures, while the other side is under ambient condition [7]. To simulate the fire condition, one-side heating tests were conducted

on UHPC slabs with the dimension of 400×400×60 mm$^3$. Note that the width of the specimens is over six times the thickness to meet the requirements of unidirectional heat transfer [44]. The heating process of the furnace followed the standard ISO 834 curve (see Fig. 2b) [40]:

$$T = 20 + 345\log_{10}(8t + 1) \quad (1)$$

where $T$ and $t$ denote the temperature ($^o$C) and heating time (min), respectively.

By covering the mouth of muffle furnace with UHPC slab, only one side of the slab (i.e., heating surface) was exposed to elevated temperatures, while the other side (i.e., measured surface) was under ambient temperature, as illustrated in Fig. 3a. The K-type thermocouples were embedded in UHPC slabs during casting with the distance from temperature measuring points to the heating surface being 0, 20, 40 and 60 mm. In addition, the temperature measuring points were filled with copper powder to guarantee good contact between thermocouples and UHPC slabs. During one-side heating tests, the temperature variations at different positions of UHPC specimens were measured by K-type thermocouples and recorded by Data Taker modules every 2 s, and the temperature distribution is presented in forms of temperature-time and temperature-position curves.

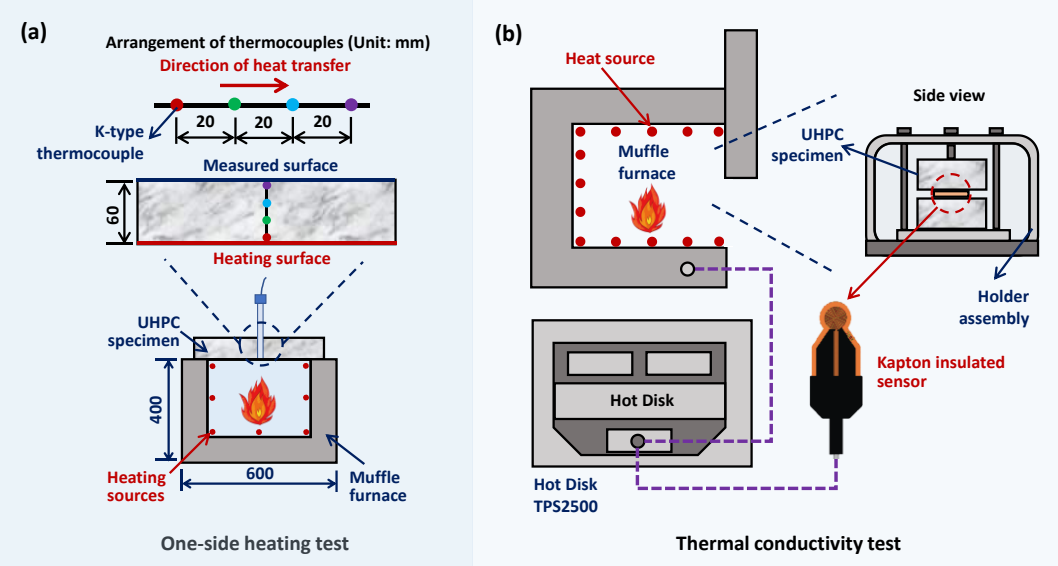


**Fig. 3.** Illustration of test setup of (a) one-side heating test, and (b) thermal conductivity test.

2.4.3. Thermal conductivity test

Currently, there is still lack of a standard test procedure for measuring the thermal conductivity of concrete at elevated temperatures [45]. Herein, the transient plane source (TPS) approach was adopted for evaluating the thermal conductivity of UHPC specimens at elevated temperatures up to 800 $^o$C as per previous studies [26,46]. The TPS measurements were conducted using a thermal constant analyser (Hot Disk, TPS-2500S, Sweden) to obtain the thermal resistance of a transiently heated plane sensor in a rapid manner. Before TPS measurement, each UHPC specimen with the dimension of 100×100×100 mm$^3$ was cut into two identical pieces, and the cutting surfaces were smoothly polished to ensure the good contact between the specimens and sensors. During the test, a Mica sensor with the radius of 6.4 mm was fitted between two pieces of UHPC specimens (i.e., 100

mm on side and 50 mm in thickness), and the specimens were placed in a muffle furnace, as shown in Fig. 3b. Firstly, the thermal conductivity of UHPC specimen at ambient temperature was measured with TPS method. Afterwards, the furnace heated up to the next temperature at a pace of 10 $^{o}$C/min and maintained at that temperature until the thermal equilibrium. Then, the thermal conductivity of specimen was measured, after which the furnace was heated up again to the following target temperature and repeated the former procedures. The target temperatures varied from 200 to 800 $^{o}$C with an interval of 200 $^{o}$C. TPS measurements were repeated three times at each temperature level to make sure the reliability of test results. Additionally, the thermal conductivity of SFRP fibres was also measured using the TPS method by shaping fibres into standard slices [47]. The maximum measurement temperature was 150 $^{o}$C to ensure the solid state of samples.

2.4.4. Confocal laser scanning microscopy

The morphology of SFRP fibre reinforced UHPC after heat exposure was detected by confocal microscopic analysis. After the compression test, crushed FRC-MP02 specimens were cut and polished to obtain a surface with relatively complete SFRP fibres. The non-contact 3D laser confocal scanning microscope (KEYENCE, VK-X1000, Japan) was then applied to carry out microscopic characterisation. As the size of SFRP fibre was too large to present in one image, local images were taken and spliced together to get a complete overview.

2.4.5. Electron probe micro analysis

The effect of SFRP fibres on element distribution of UHPC was evaluated through electron probe micro analysis. Herein, only the specimens exposed to 600 $^{o}$C for 2 h prior to compression test were selected to demonstrate the final distribution of elements at elevated temperatures. Before the EPMA measurement, selected samples were cast in epoxy resin and polished to obtain flat surfaces (roughness < l μm) [48]. Afterwards, five main elements (i.e., Si, O, Ca, Al and Mg) were detected using a micro electron probe (Shimadzu, EPMA-1720, China), and the contour maps of element distribution were plotted in terms of the weight percentage.

2.4.6. Mercury intrusion porosimetry

MIP was employed to characterise the pore size distribution of UHPC specimens at elevated temperatures. Small samples (less than 500 mm$^3$) were taken from the cores of UHPC specimens so that no significant microstructural damage was induced by compressive tests. After oven drying for 24 h, MIP test was performed using a mercury porosimeter (Micromeritics, Auto Pore IV 9500, USA) with the applied intrusion pressure varying from 5 KPa to 350 MPa, and the equivalent pore size was derived from the applied pressure based on the Washburn equation [49].

2.4.7. Nanoindentation

The micromechanical properties of UHPC specimens after exposure to elevated temperatures were measured through nanoindentation tests. The load-displacement curves of different phases and the corresponding SEM images of tested zones were obtained simultaneously using a nanoindentation

indenter with top surface referencing technique (Anton Paar, NHT, Austria). The nanoindentation test began with linear loading under a constant rate of 300 mN/min until the maximum load of 50 mN was reached. Afterwards, the load at the maximum level was held for 5 s, followed by unloading with a constant rate of 300 mN/min. The average indentation depth was as deep as 2000 nm to avoid the influence of surface roughness on measurement [50].

## 3. Characteristics of synthetic flame-retardant polymer fibres

### 3.1. Chemical composition

Fig. 4 shows the XRD patterns of OP and MP fibre at ambient temperature, indicating that the main XRD spectra of two types of SFRP fibres are similar. As seen in Fig. 4a, the four typical peaks within the $2\theta$ range of 10–25° can be attributed to the melting of PP resin matrix [51]. The intensive diffractions ranging from 25° to 30° can be explained by the organic intumescent flame retardants, including APP, MEL and PER [35]. In particular, the additions of metallic fillers in MP fibre results in the prominent peaks at $2\theta$ of 18.4° and 38.0° [36], as displayed in Fig. 4b. Therefore, the characteristic crystals of raw materials in synthetic flame-retardant polymer fibres can be reserved after the melting extrusion and cooling moulding processes.

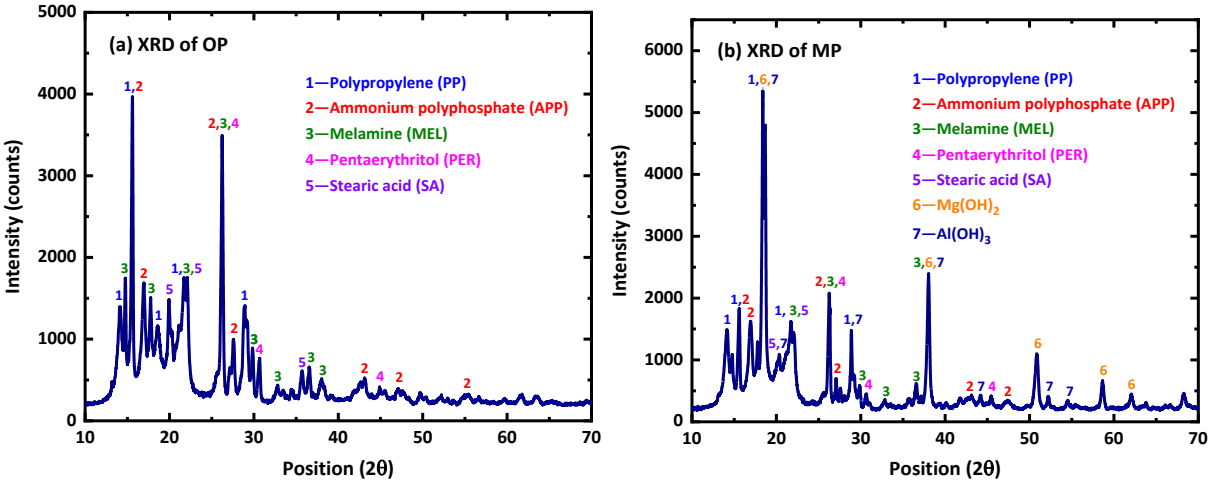


**Fig. 4.** X-ray diffractions of (a) OP and (b) MP fibres.

### 3.2. Molecular structure

Fig. 5 illustrates the FTIR spectra of SFRP fibres at both ambient and elevated temperatures, where the intense stretching vibrations can be divided into four ranges for both OP and MP fibres. (i) At ambient temperature, the distinctive absorptions peaking at 3300–3500 $cm^{-1}$ represent the amino groups (-NH) of APP and MEL and the hydroxyl groups (-OH) of PER [52]. However, these absorptions are greatly weakened at elevated temperatures due to the melting polycondensation between APP and PER. The left peak at 3418 $cm^{-1}$ can be attributed to the amino groups (-NH) of pyrophosphoric acid and polyphosphoric acid in the residue substance [53]. (ii) The stretching vibrations of -CH bonds (2800–3000 $cm^{-1}$) and bending vibrations of -$CH_2$ bonds (around 1550 $cm^{-1}$) keep shifting to lower frequency sharply with elevated temperatures due to the breaking of chain structures in PP resin [54]. (iii) The distinctive double absorption peaks between 1640 and 1436

$cm^{-1}$ are associated with the stretching vibrations of C=N and C-N in MEL, which remains in the spectra of residual substance at up to 400 °C [55]. (iv) The absorption peaks between 1000 and 1100 $cm^{-1}$ are related to the characteristic vibrations of $PO4^{3-}$ groups. The stretching vibrations of P-O-P and P-O-H in polyphosphate chains lead to absorption peaks ranging from 600 to 950 $cm^{-1}$ [56]. Therefore, the molecule structural characteristics of both OP and MP fibres are similar. The decomposition and esterification reactions of organic flame retardants can be considered as the main reasons for phase transformations of SFRP fibres at elevated temperatures [52].

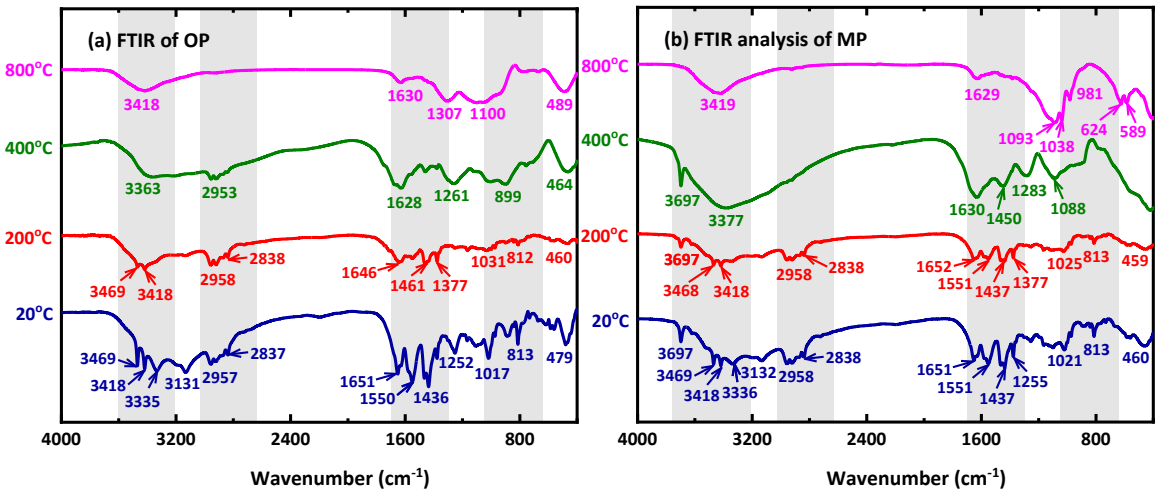


**Fig. 5.** FTIR spectra of (a) OP and (b) MP fibres at elevated temperatures.

### 3.3. Thermal stability

A comparison of the heat release rate of two types of SFRP fibres is shown in Fig. 6. There is no obvious difference between them in terms of temperature at which the maximum heat release rate takes place, i.e., around 477 °C and 478 °C, respectively. However, the incorporation of $Mg(OH)_2$ and $Al(OH)_3$ greatly restrains the flammability intensity of SFRP fibres. The maximum heat release rate decreases significantly from 933.9 W/g to 649.7 W/g with the addition of metallic fillers, suggesting that metal hydroxides have promoting effect on the thermal stability of SFRP fibres [36].

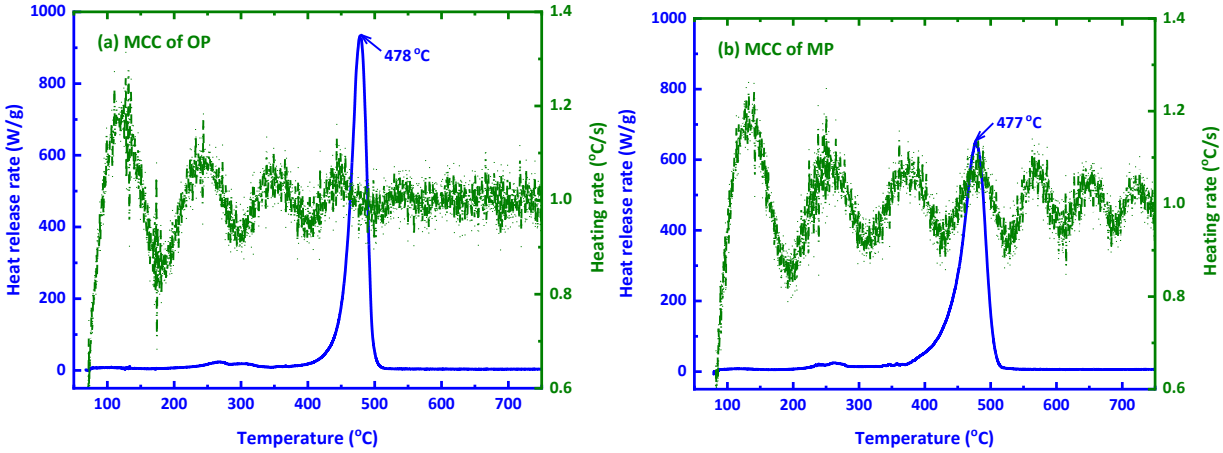


**Fig. 6.** MCC analysis of (a) OP and (b) MP fibres.

The TG and DTG (first derivative of TG) curves of SFRP fibres are displayed in Fig. 7. OP fibre experiences an 80.05% mass loss with the increase of temperature from 162 to 484 °C.

Similarly, the mass loss of MP fibre is 77.44 % between 161 and 491 °C. Thus, they share similar effective temperature ranges, during which the char formation reactions among organic intumescent flame retardants take place. The DTG curve in Fig. 7a suggests four peaks of mass loss rate for OP fibre. The first two peaks within 220–280 °C can be attributed to the decompositions of acid source (i.e., APP) and carbon source (i.e., PER), and the liberated phosphoric acid and non-flammable gases trigger the first series of reactions [57]. Followed by the dehydration of nitrogen source (i.e., MEL) at around 300–440 °C, a carbon-like foam layer is formed over the polymer substrate and the maximum reaction rate can be reached with an endothermic peak at 419 °C [34]. The last peak at 910 °C can be ascribed to the further carbonization of phosphorous oxynitrides in foam layers [52]. In comparison with Fig. 7a, the TG curve of MP fibre shown in Fig. 7b has three main differences. Firstly, the first two peaks at 221 and 251 °C are replaced by one peak at 299 °C. This is because both APP-PER char formation and decomposition of MEL occur within the same temperature range [58], and thus the first two peaks may coincide with each other. Besides, the temperature corresponding to the maximum reaction increases from 419 to 457 °C with the presence of $Mg(OH)_2$ and $Al(OH)_3$, indicating that metallic fillers can inhibit the decomposition of flame retardants [59]. Moreover, the final left mass of MP fibre (19.52%) is higher than that of OP fibre (12.88%), because of the thermal stability of decomposed metallic fillers (i.e., MgO and $Al_2O_3$).

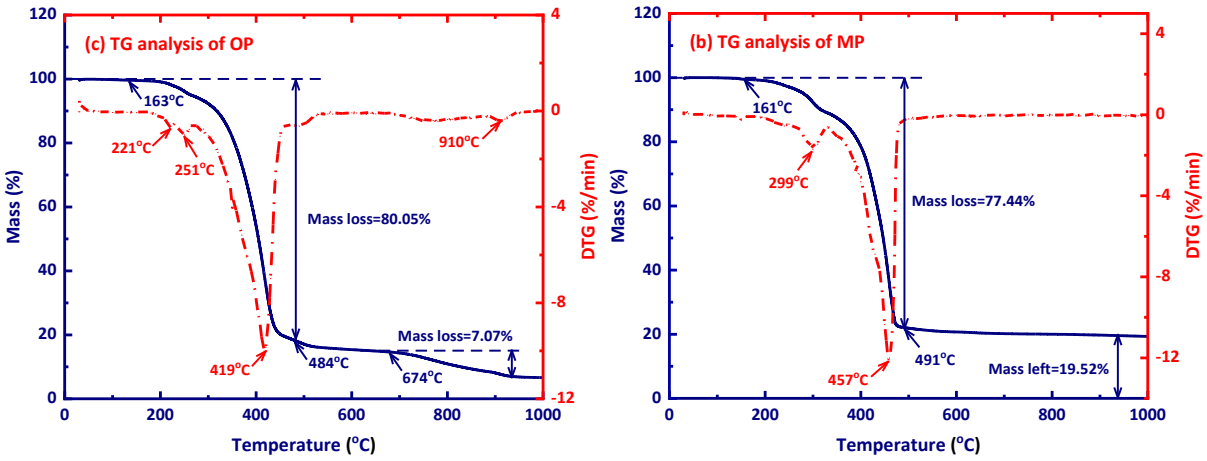


**Fig. 7.** TG curves and their differential forms of (a) OP and (b) MP fibres.

The DSC curves shown in Fig. 8 provide more insights into the thermal reactions of SFRP fibres. The presence of first endothermic peak at 152 °C can be attributed to the melting of polymer resin and transformation of crystal structures, which corresponds to the starting point of mass loss in TG curves. With the increase of temperature, APP begins to decompose and initiate the esterification of PER (i.e., dehydrating and dehydrogenizing intra-molecularly [60]), leading to the characteristic peaks around 254 °C (Fig. 8a). The generated acid from APP promotes the dehydration of MEL and the further char formation reactions. Accordingly, two endothermic peaks can be observed at 411 and 447 °C, which agree with the temperature of maximum mass loss rate in TG curves. For OP fibres, the foaming products of organic intumescent flame retardants can be

gradually oxidized to carbon dioxide, leading to the presence of an exothermic peak at over 600 °C [52]. In contrast, several intensive characteristic peaks at over 700 °C disappear in the DSC curve of MP fibres, as shown in Fig. 8b. This can be ascribed to the presence of metal hydroxide fillers, which not only inhibits the thermal decomposition of organic foams but also promotes the thermal stability of MP fibres [59], resulting in higher residual mass at elevated temperatures, as confirmed by the TG results in Fig. 7.

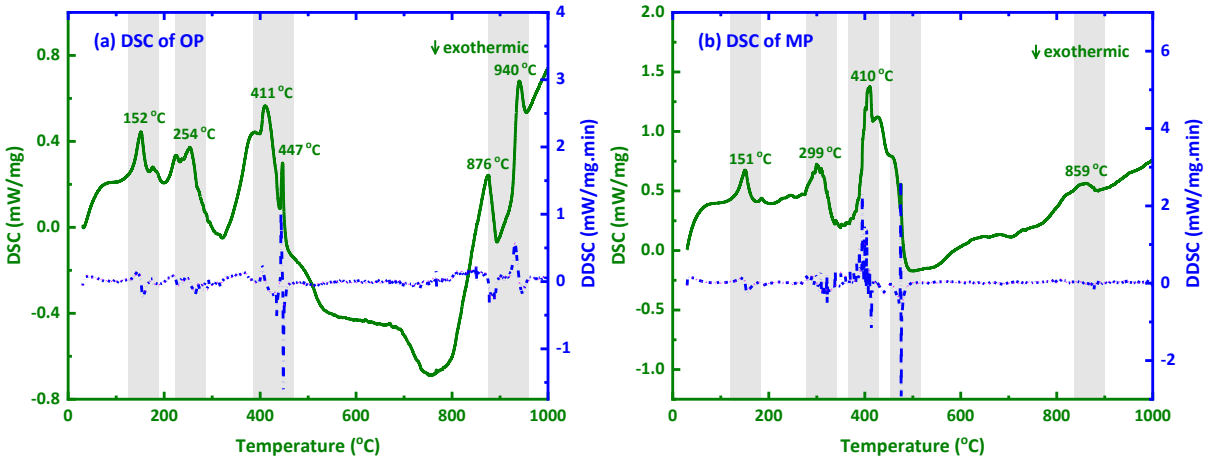


**Fig. 8.** DSC curves and their differential forms of (a) OP and (b) MP fibres.

### 3.4. Micromechanical properties

Fig. 9 demonstrates the morphology analysis of SFRP fibres at ambient temperatures. Topographic height images of synthetic flame-retardant polymer fibres are presented in Fig. 9a and b, where the interlacing light and dark lines stand for convex and concave, respectively. The tube-like inclusions are surrounded by smooth polymer matrix, and there is no obvious change of topography by adding metallic fillers. Mapping images of elastic modulus are plotted in Fig. 9c and d, in which the darker colour bar is, the lower value of modulus is. Note that SFRP fibres are in a solid state at the measured temperature, and thus the elastic modulus can be applied to characterise fibre surface properties. Because of the addition of metallic fillers, the average elastic modulus of MP fibre (4.55 GPa) is over three times higher than that of OP fibre. Fig. 9e and f illustrate the adhesion of SFRP fibres in the form of topographic mapping, and the colour of image is consistent with that of the modulus map. The addition of metallic fillers results in a 66.42% increase of the average adhesion for MP fibre compared to that for OP fibre. The statistical analysis of adhesion results (Fig. 9g and h) also indicates that MP fibre has a higher probability density function of adhesion (around 50–65 nN) than that of OP fibre (around 20–40 nN). Thus, $Mg(OH)_2$ and $Al(OH)_3$ can help enhance the micromechanical properties of SFRP fibres and a higher modulus and adhesion can be achieved. Generally, the incorporation of polymer fibres such as PP, PVA and PE fibres would lead to the strength loss of UHPC due to their relatively low elastic modulus [4]. Therefore, the enhanced mechanical properties of SFRP fibres would help reduce the strength loss induced by polymer fibres, which will be discussed in detail below.

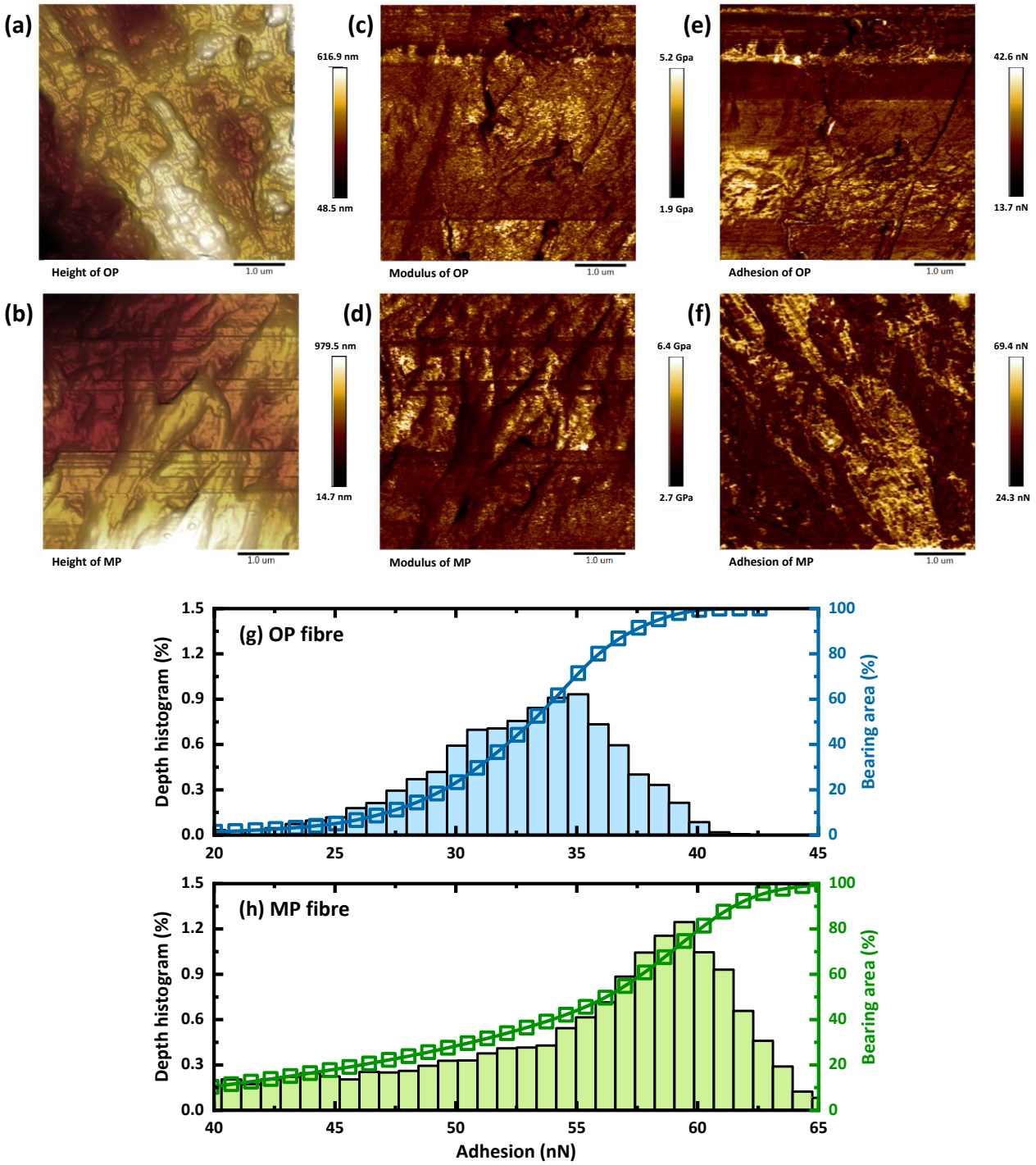


**Fig. 9.** (a)–(f) AFM topographies of height, elastic modulus, and adhesion of OP and MP fibres, and (g) and (h) statistical analysis of the adhesion results.

## 4. Thermal and mechanical behaviour of SFRP fibre reinforced UHPC

### 4.1. Mass loss

Fig. 10 presents the variation of mass loss with temperature for all mixtures in comparison with their masses before heating. The corresponding appearances of UHPC specimens after exposure to elevated temperatures are shown in Fig. 11. In general, the higher the temperature, the more the mass loss and the darker the colour of specimens. According to previous studies, the mass loss curves can be divided into four stages [26,61], which is adopted in the following discussion.

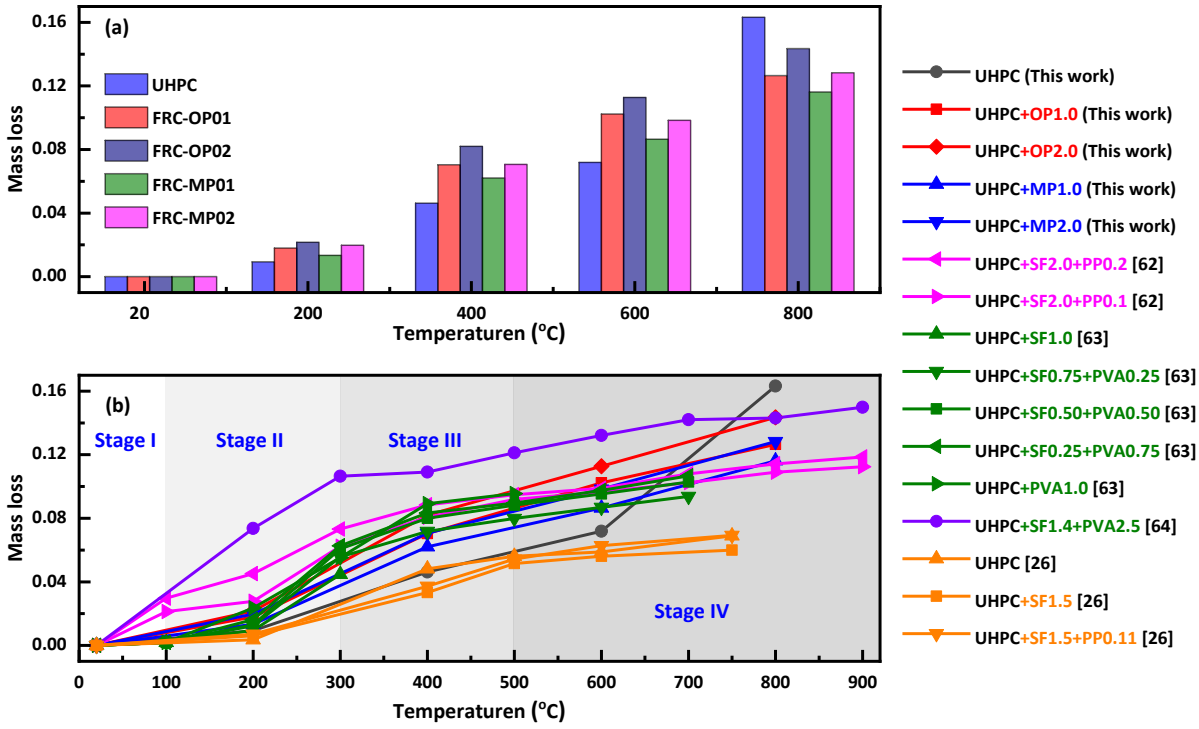


**Fig. 10.** (a) Mass loss of SFRP fibre reinforced UHPC, and (b) comparisons with previous studies [26,62–64] (Note: SF – steel fibre, PP – polypropylene, PVA – polyvinyl alcohol, SF0.75+PVA0.25 – volume fractions of steel and PVA fibres of 0.75% and 0.25%, respectively).

In Stage I (20–100 °C) only small initial mass loss can be observed due to the evaporation of free water present in UHPC matrix. The w/b ratio of UHPC is relatively lower than normal concrete, leading to a more dense microstructure of UHPC and considerably less free water in UHPC [62]. In general, the average mass loss by previous studies and this study is less than 2% of the total weight. The evaporation of leftover free water and physically absorbed water results in a further mass loss in Stage II (100–300 °C) [63]. Besides, SFRP fibres start to melt at around 165 °C (see Fig. 7), leading to an additional mass loss. Similarly, the melting of traditional polymers, i.e., PVA fibres and PP fibres, would also result in further mass loss of UHPC. Therefore, the mass loss of SFRP fibre reinforced UHPC over this stage is consistent with the previous findings [26,62,63]. In Stage III (300–500 °C), $Ca(OH)_2$ decomposes into CaO and $H_2O$ providing more available water, and the evaporation of decomposed water and chemically bound water causes a rapid mass loss [64]. In addition, the mass loss increases with the increasing SFRP fibre content due to the evaporation of polymer matrix and foaming reactions of APP-PER-MEL in SFRP fibres, which provides more channels for moisture evaporation (Fig. 11c) and accelerates the mass loss rate of UHPC matrix during this stage. When the temperature exceeds 500 °C, in Stage IV, the explosive spalling of UHPC takes place (Fig. 11d), resulting in a sharp mass loss. The mass loss during this stage can be ascribed to the complete evaporation of the present water. Moreover, the carbonization and evaporation of SFRP fibres would induce further mass loss over this stage [26], and thus higher mass loss occurs in UHPC specimens than previous results, as shown in Fig. 10b. In addition, OP

fibre results in a more obvious mass loss of UHPC specimens than MP fibre at the same dosages, which can be explained by (i) The addition of metallic fillers improves the thermal stability of MP fibre as discussed in Section 3.3, and the thermal degradation of OP fibre is faster than MP fibre. (ii) The foaming reactions of SFRP fibres can lead to the formation of carbon-like insulation layer over heating surfaces, which blocks the heat transfer within UHPC matrix. The metallic additives promote the foaming efficiency of MP fibres and the formation of insulation layer (Fig. 11e), and accordingly slows down the mass loss rate of UHPC at elevated temperatures.

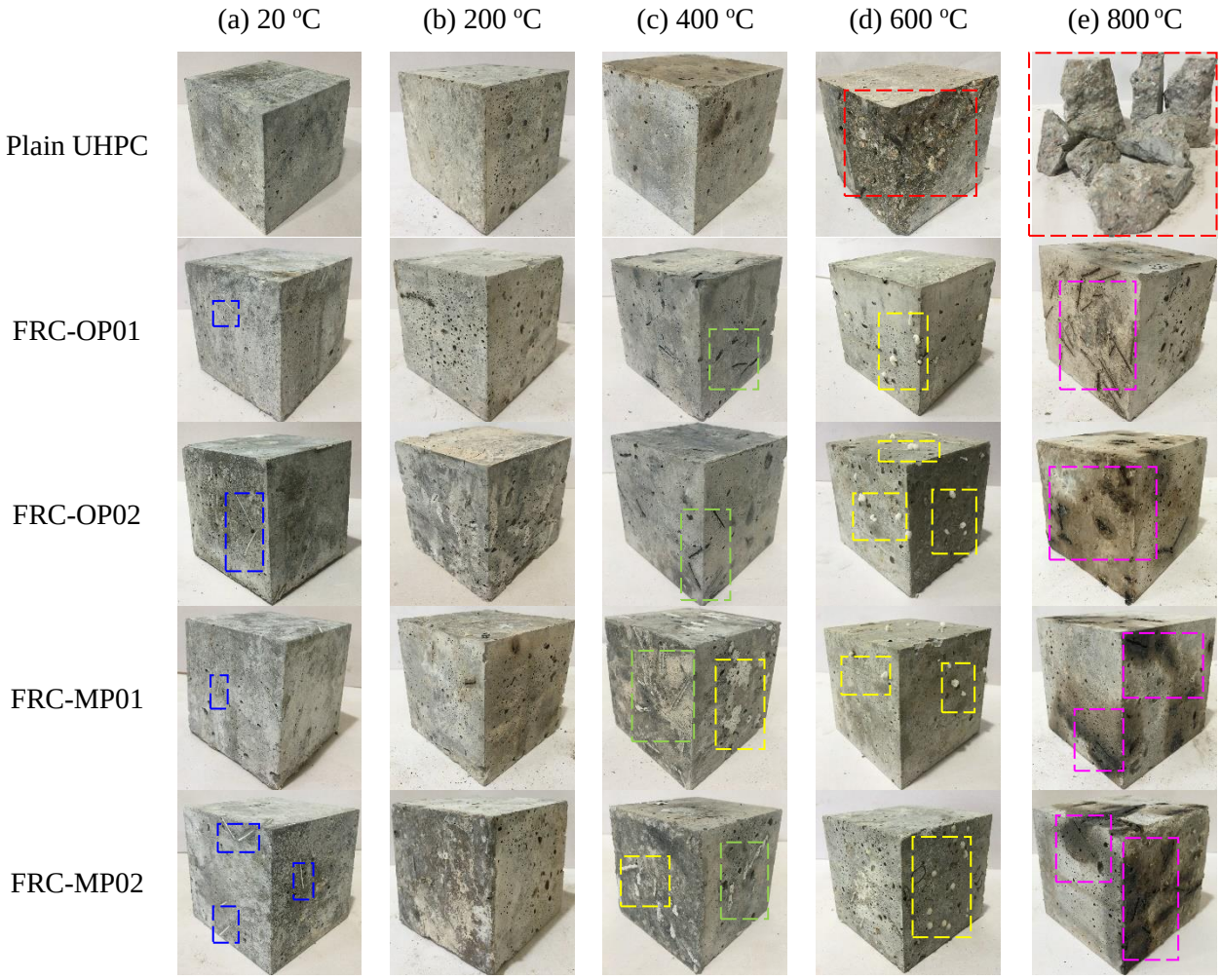


**Fig. 11.** Appearances of plain UHPC and SFRP fibre reinforced UHPC at elevated temperatures (legend of outlines: blue – SFRP fibres, green – melted SFRP fibres, yellow – foaming products, red – explosive spalling, pink – char formation).

### 4.2. Compressive behaviour

4.2.1 Stress-strain curves

The uniaxial compressive stress-strain curves of UHPC reinforced with SFRP fibres are plotted in Fig. 12a–d. Overall, the typical stress-strain curves can be roughly divided into two stages, i.e., an increasing stage reaching the peak stress and a decreasing stage approaching a relatively stable value of the residual stress [65]. With the increase of temperature, the peak stress decreases gradually, and so does the ascending rate before reaching the peak stress. Similarly, the descending

rate approaching to the residual stress also decreases with the increasing temperature, implying the extended post-peak softening behaviour at elevated temperatures [66].

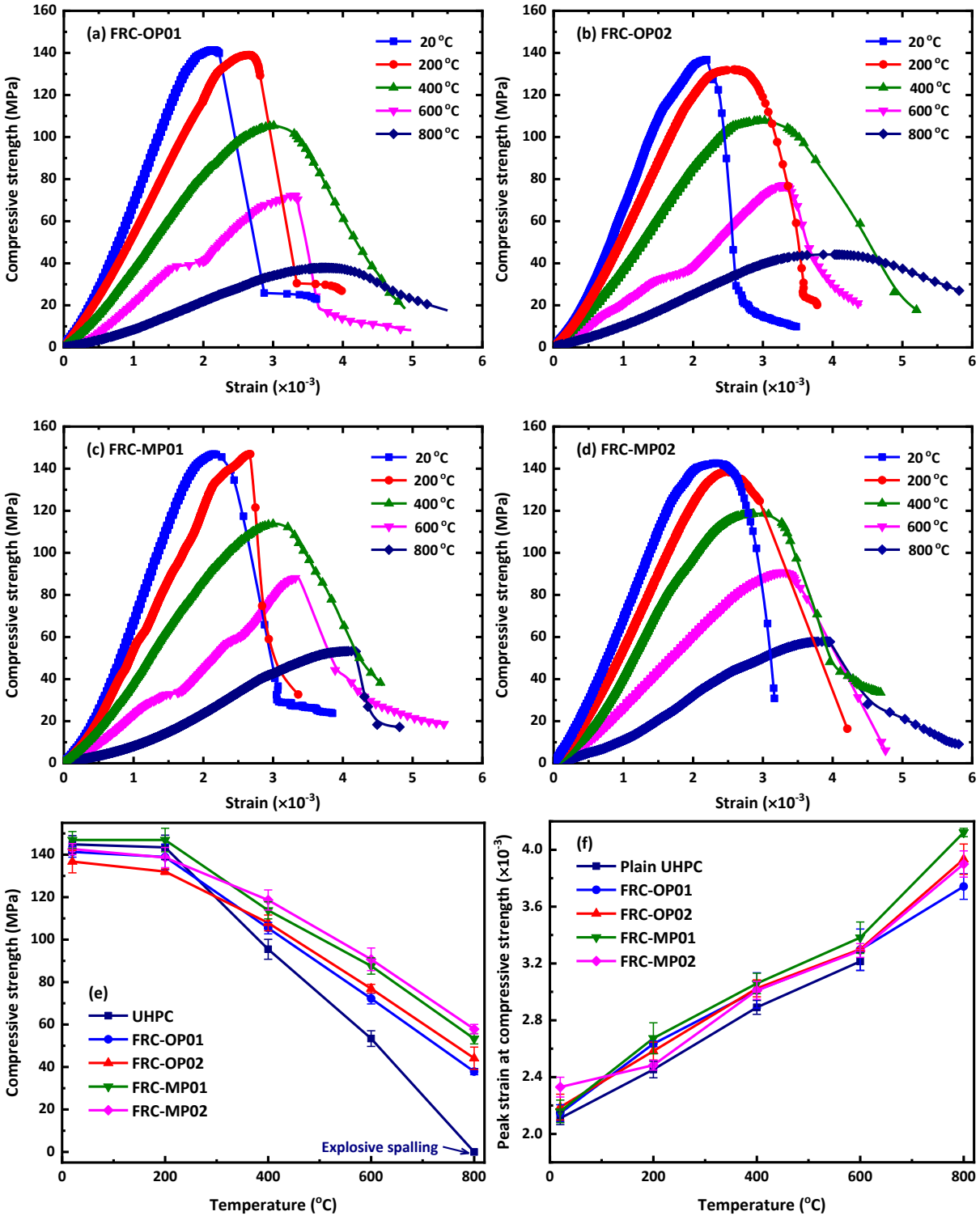


**Fig. 12.** (a)–(d) Uniaxial compressive stress-strain curves of SFRP fibre reinforced UHPC, and (e)–(f) Compressive strength and the corresponding peak strain at various temperatures.

The compressive strength and the corresponding peak strain of UHPC specimens at various temperatures are summarised in Fig. 12e and f. At ambient temperature, increasing the OP fibre content from 1.0% to 2.0% causes the increase of strength loss of UHPC specimens from 2.42% to

5.59%. In contrast, UHPC reinforced with 1.0% MP fibre even exhibits a slight increase of 1.45% in compressive strength, while only 1.54% strength loss occurs when the volume fraction of MP fibre is increased to 2.0%. At elevated temperatures, both types of SFRP fibres play an important role in reducing the strength loss with temperature. The residual compressive strength is increased with the increasing SFRC fibre content, and MP fibre is more effective in retaining the compressive behaviour at elevated temperatures than OP fibre. For instance, the strength loss of plain UHPC is 38.81% and 46.75% higher than that of FRC-OP02 and FRC-MP02, respectively, when the temperature increases from 200 to 600 $^{o}$C. Moreover, the addition of SFRP fibres also leads to an increased peak strain at compressive strength, and FRC-MP01 performs the best in terms of the ductility, the peak strain of which is 5.21% higher than that of plain UHPC at 600 $^{o}$C.

4.2.2 Residual compressive strength

Fig. 13a illustrates the compressive strength of UHPC reinforced with hybrid fibres at ambient temperature. Due to the low modulus of polymer fibres, the incorporation of PE, PP, and PVA fibres has a negative effect on the compressive strength of UHPC [32,67,68]. In contrast, hybrid steel and polymer fibres can promote the compressive behaviour of UHPC under certain volume fractions [23,27]. Although the compressive strength of OP fibre reinforced UHPC is inferior to plain UHPC, the strength loss caused by OP fibre is lower than that of polymer and natural fibres under the same volume fraction. The incorporation of 1.0% PE/PVA/jute fibres can lead to over 10% strength loss of UHPC, while only less than 3% strength loss can be observed when adding 2.0% OP fibre in UHPC matrix. In addition, metallic fillers can improve the mechanical properties of MP fibre (as discussed in Section 3.4), which would further mitigate the negative influence on compressive performance of UHPC. Accordingly, the compressive strength of FRC-MP02 is 4.31% higher than that of FRC-OP02 at ambient temperature.

The changes of normalised compressive strength with elevated temperatures are presented in Fig. 13b. The curves can be divided into four stages in a similar way to Section 4.1. In Stage I, there is no obvious change of compressive strength with temperature. In Stage II, the compressive strength of normal concrete decreases significantly [69,70], while the compressive strength of UHPC reinforced with hybrid fibres drops slightly or even increases to some degree. This is because the removal of absorbed water increases the Van der Waals surface forces, and accordingly increases the compressive strength [63]. Besides, the phase changes induced by hydrothermal conditions can build up pore pressure in the dense microstructure of UHPC matrix, contributing to the further strength increase. In Stages III and VI, the evaporation of chemically bound water and decomposition of hydration products lead to a continuous decrease in compressive strength [16]. The residual compressive strength of SFRP fibre reinforced UHPC is higher than that observed for UHPC reinforced with hybrid polymer and steel fibres. The average strength loss of hybrid fibre reinforced UHPC by previous studies was found to go up from 25.79% to 57.74% while that of

SFRP fibre reinforced UHPC rises from 21.47% to 42.36% as the temperature increases from 400 to 600 °C. Among all mixtures, FRC-MP02 performs the best in terms of the residual compressive strength which remains 0.636 and 0.406 at the elevated temperatures of 600 and 800 °C, respectively, compared to that at ambient temperature. This is because the commonly used polymer fibres may evaporate at over 340 °C, and thus the effect of hybrid fibres is limited at over 400 °C [25]. In contrast, the foaming reactions of flame retardants in SFRP fibres can still lead to the formation of carbon-like layer over this temperature range, which not only slows down the heating rate of specimens but also enhances the residual compressive strength of UHPC.

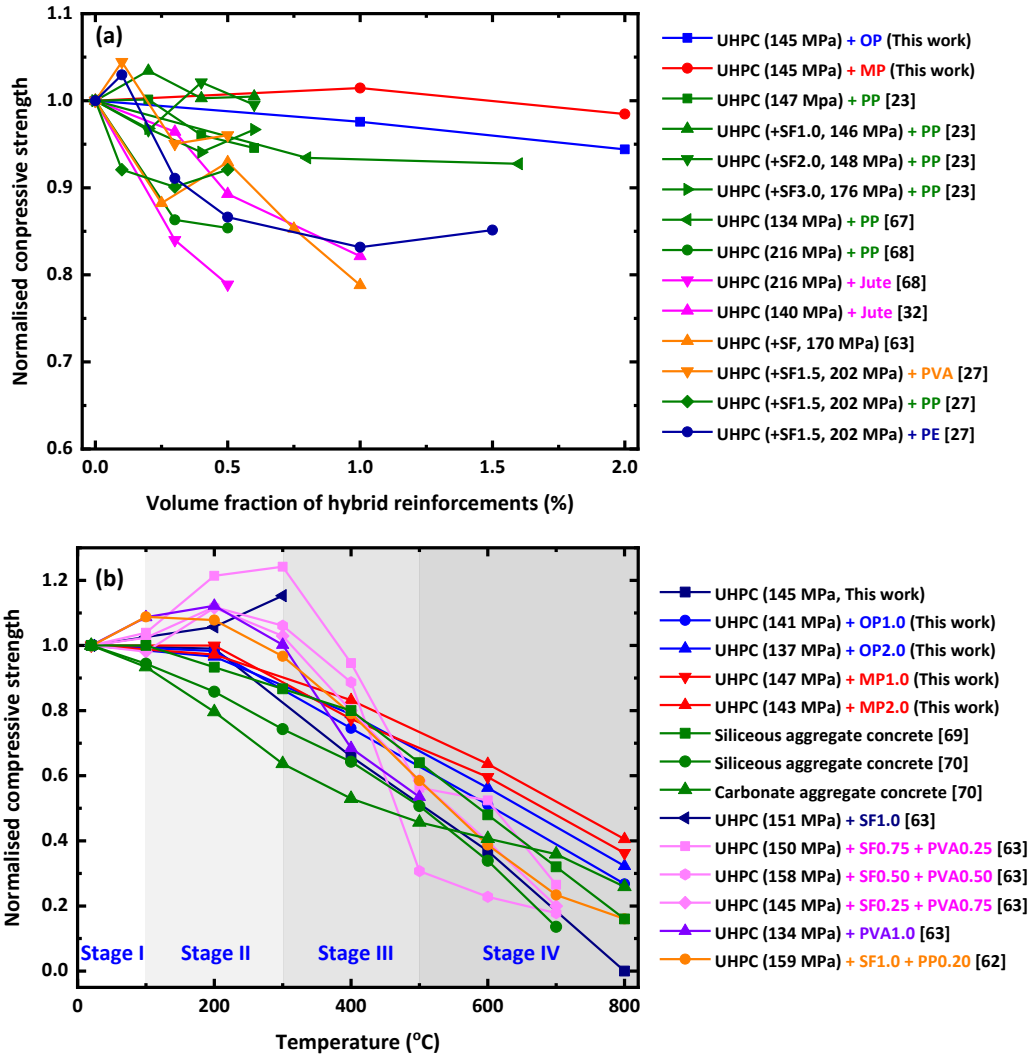


**Fig. 13.** Compressive strength of UHPC reinforced with hybrid fibres at (a) ambient temperature [23,27,32,63,67,68] and (b) elevated temperatures [62,63,69,70] (Note: the marked strength in legend of (a) represents the compressive strength of plain UHPC, while it means the compressive strength of fibre reinforced UHPC at ambient temperature in (b); PE – polyethylene).

4.2.3 Elastic modulus

The temperature-dependent elastic modulus is a key parameter for evaluating the degradation of mechanical properties of concrete structures. In this study, the elastic modulus of UHPC is calculated based on the secant modulus at half of the peak load extrapolated from the uniaxial

compressive stress-strain curves [66]. Table 6 presents the relative elastic modulus at various temperatures. Overall, there exists a similar effect of temperature on the modulus of elasticity to that on the residual compressive strength. Although the incorporation of OP fibre can result in a slight loss of elastic modulus at ambient temperature, UHPC reinforced with 1.0% MP fibre even shows a 2.76% higher elastic modulus compared with plain UHPC. Plain UHPC experiences a 27.4% loss of elastic modulus at 200 °C, while its compressive strength decreases slightly or even increases at this temperature level (Fig. 12e). This can be explained by the increase of peak strain at compressive strength (Fig. 12f), and accordingly the ascending rate of strain-stress curves before reaching the peak stress decreases. Moreover, the elastic modulus of plain UHPC reduces dramatically to about a half (0.501) at 400 °C and less than a quarter (0.219) at 600 °C. In contrast, the incorporation of SFRP fibres delays the elastic modulus reduction of UHPC at elevated temperatures. The increase of SFRP fibre content brings a positive effect on the residual elastic modulus. For instance, about three quarters (0.731) of elastic modulus is retained at 400 °C and more than a half (0.552) is held at 600 °C for FRC-MP02. Therefore, MP fibre can improve the elastic modulus of UHPC at ambient temperature and contribute to the retaining of elastic modulus at elevated temperatures. The optimal SFRP fibre content of 2.0 vol% is recommended considering the strength loss of UHPC subjected to elevated temperature.

**Table 6** Variation of elastic modulus of UHPC mixtures with elevated temperatures.

| Temperature (°C) | | Plain UHPC | FRC-OP01 | FRC-OP02 | FRC-MP01 | FRC-MP02 |
|---|---|---|---|---|---|---|
| 20 | EM (GPa) | 47.90±2.79 | 46.65±2.96 | 42.12±2.70 | 49.22±3.06 | 47.70±3.96 |
| | RV20 | 1 | 1 | 1 | 1 | 1 |
| 200 | EM (GPa) | 34.80±2.29 | 38.60±2.87 | 39.32±2.63 | 45.14±2.84 | 45.35±2.63 |
| | RV20 | 0.726 | 0.828 | 0.934 | 0.917 | 0.951 |
| 400 | EM (GPa) | 23.97±2.47 | 27.95±1.66 | 29.81±1.49 | 31.63±2.14 | 34.87±2.91 |
| | RV20 | 0.501 | 0.599 | 0.708 | 0.643 | 0.731 |
| 600 | EM (GPa) | 10.48±2.22 | 19.77±1.50 | 22.49±1.38 | 23.59±1.77 | 26.31±2.04 |
| | RV20 | 0.219 | 0.424 | 0.534 | 0.479 | 0.552 |
| 800 | EM (GPa) | 0 | 10.81±0.97 | 12.87±0.62 | 14.41±1.02 | 16.98±1.17 |
| | RV20 | 0 | 0.232 | 0.305 | 0.293 | 0.356 |

Note: EM – elastic modulus; RV20 means the relative value compared with the EM at ambient temperature.

#### 4.2.4 Failure modes

Fig. 14 illustrates the typical failure modes of SFRP fibre reinforced UHPC under uniaxial compression. In general, all UHPC specimens present shear failure, and the type and content of SFRP fibres have insignificant effect on the failure mode. Before reaching the peak stress, no apparent cracks appear on the surface of UHPC specimens. As long as the peak stress is reached, visible cracks initiate at the corner of specimen followed by a slight explosion, and then diagonally expand across the section forming an X-shaped shear plane [71]. The propagation angle between

shear plane and vertical direction is approximately 45°, and the wedge blocks may cause a relative slip along the shear plane with the further increase of deflection [66]. At ambient temperature, SFRP fibres can delay this shear sliding because of the bridging and anchoring effects, leading to better integrity of the specimen [42]. As seen in Fig. 14a, some MP fibres on the shear surface are pulled out from the UHPC matrix in FRC-MP02, resulting in a gradual loss of load-bearing capacity rather than the brittle failure of specimen. With the increase of exposure temperature, UHPC matrix becomes more fragile due to the decomposition of cement hydrates, and the increase of shear sliding makes the specimen gradual lose its integrity [72], as displayed in Fig. 14(b)–(e). Moreover, SFRP fibre reinforced UHPC has better integrity than plain UHPC, which can be ascribed to the foaming of intumescent flame retardants and formation of carbon-like layer that slows down the loss of moisture and decomposition of hydrated products. Thus, the specimens containing SFRP fibres are more ductile and less fragile than plain UHPC at elevated temperatures.

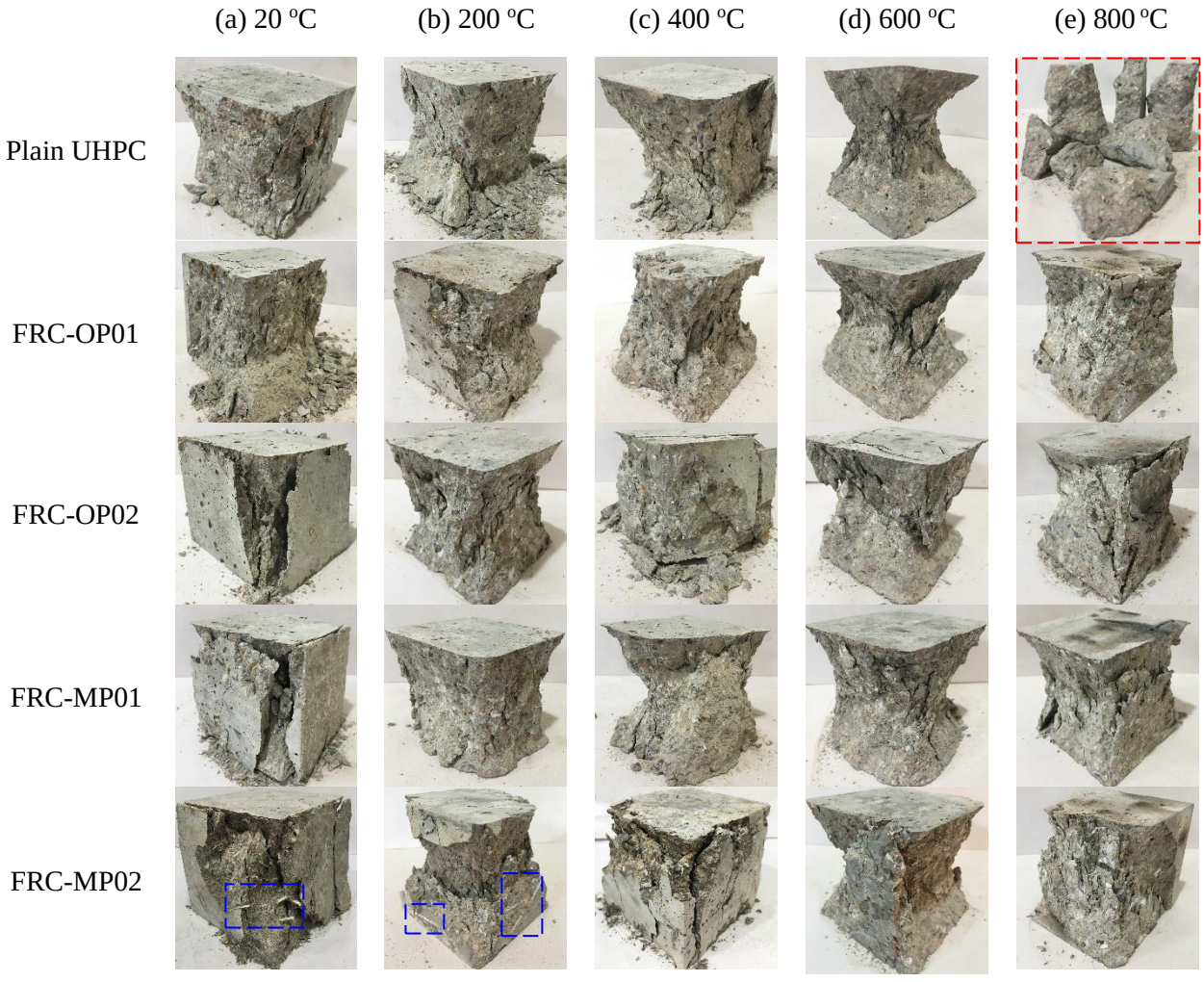


**Fig. 14.** Failure modes of UHPC specimens with/without SFRP fibres under uniaxial compression.

### 4.3. Temperature distribution

Based on the measured time- and position-dependent temperature curves, Figs. 15a–e display the temperature contour maps of UHPC slabs under one-side heating. Obviously, the temperature increasing rate slows down in FRC slabs, and the temperature gradient across the UHPC slabs is

also decreased by adding SFRP fibres. For instance, the maximum temperature of plain UHPC slab reaches as high as 648 °C, while the highest temperature of heating surface of FRC-OP02 and FRC-MP02 slabs is only 518 and 473 °C, respectively. In addition, the highest temperature difference of plain UHPC slab is 15.41% higher than that of FRC-MP02 at the end of heating test. It is worth noting that the decreasing temperature gradient helps prevent the formation of thermal stress-induced cracks in UHPC matrix [14], which is beneficial to the mechanical properties of UHPC.

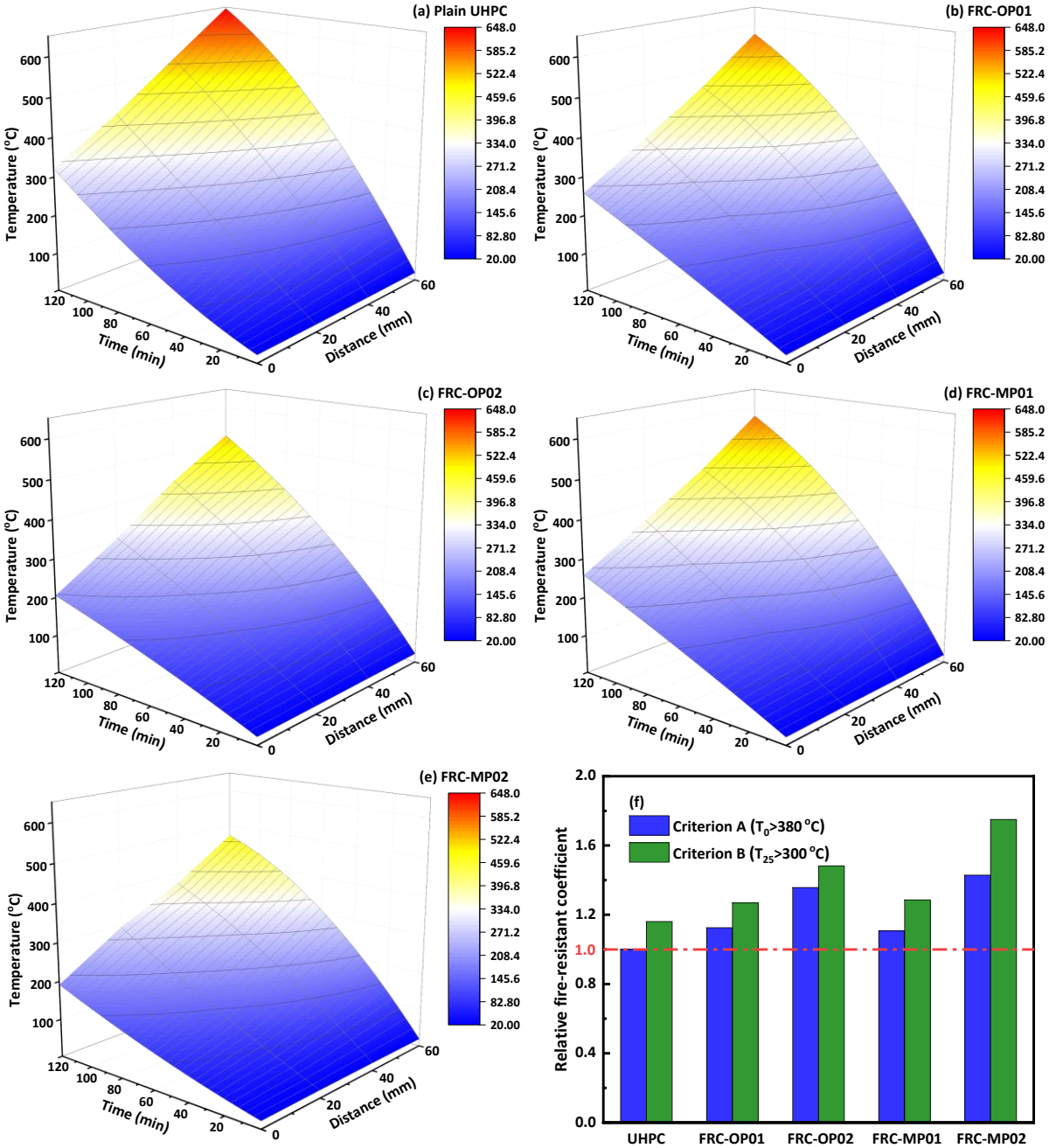


**Fig. 15.** (a)–(e)Temperature distribution of UHPC slabs at different distances from the measured surface, and (f) relative fire resistance coefficient of them against different criteria.

Further quantitative analysis is made by defining $T_0$ =300 °C (i.e., criterion A) and $T_{25}$ =380 °C (i.e., criterion B) as two criteria for fire resistance limit of UHPC slabs, where $T_i$ denotes the temperature of a position along the distance of $i$ mm to the heating surface [73]. In this study, the

time required for plain UHPC slab to meet criterion A is regarded as the lower time limit of fire resistance, and the relative fire-resistant coefficient is calculated as the relative time needed to satisfy each criterion, as presented in Fig. 15f. Generally, criterion A is more rigorous compared with criterion B, and the relative fire-resistant coefficient of SFRP fibre reinforced UHPC slabs is higher than that of plain UHPC slab under both criteria regardless of the fibre type and volume fraction. The promoting effect of SFRP fibres on fire resistance of UHPC becomes obvious with the increasing fibre content. The relative fire-resistant coefficient of FRC-OP specimens has a 20.63% and 16.99% increase under criteria A and B, respectively, as the content of OP fibre increases from 1.0% to 2.0%. Moreover, MP fibre reinforced UHPC slabs exhibit better fire resistance than UHPC incorporated with OP fibre under the same fibre content. FRC-MP02 performances the best in terms of both criteria with the relative fire-resistant coefficients of 5.25% and 18.07% higher than that of FRC-OP02 under criteria A and B, respectively. Thus, the addition of both types of SFRP fibres can enhance the fire resistance of UHPC, while MP fibre is more effective in prolonging the time to reach the fire-resistant limits of UHPC slabs.

### 4.4. Thermal conductivity

Fig. 16a shows the thermal conductivity of two types of SFRP fibres measured using TPS method. The melting point of SFRP fibres is around 165 °C as indicated in the TG analysis (Fig. 7). Thus, the maximum measurement temperature was set as 150 °C to ensure the solid state of polymer fibres [47]. The thermal conductivity of both types of fibres is in the range of 0.26–0.36 W/m·K. The elevated temperature has insignificant effect on the thermal conductivity over the measured temperature range. Besides, MP fibre has a higher thermal conductivity than OP fibre, which can be ascribed to the high conductivity of $Mg(OH)_2$ and $Al(OH)_3$ [74]. Fig. 16b illustrates the measured thermal conductivity of SFRP fibre reinforced UHPC at elevated temperatures, which suggests a downward trend with increasing temperature. The thermal conductivity of plain UHPC decreases significantly from 2.08 to 1.22 W/m·K when the temperature rises from 20 to 800 °C, and the incorporation of SFRP fibres further decreases the thermal conductivity of UHPC specimens.

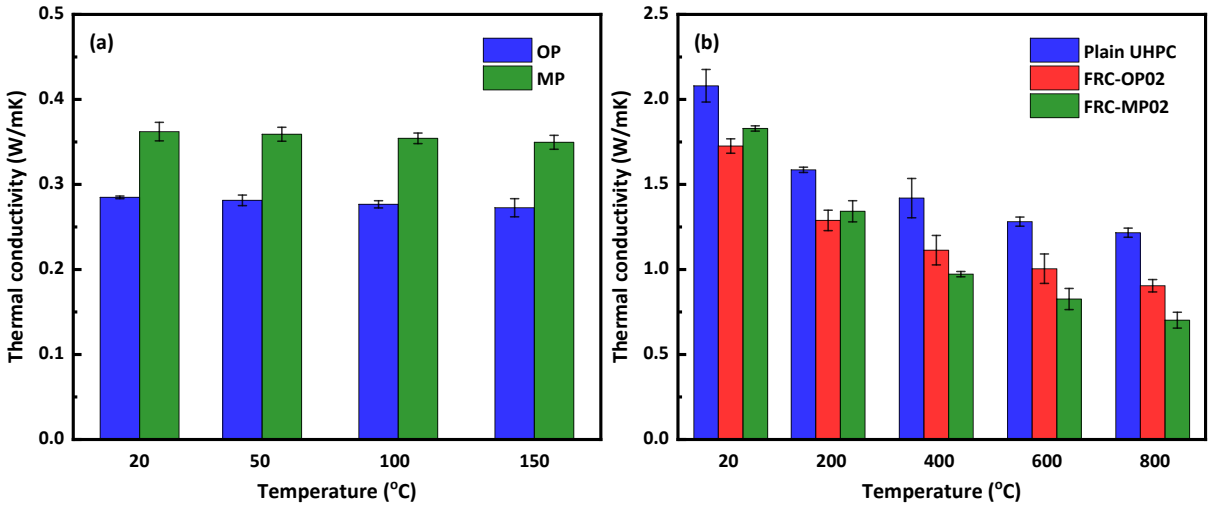

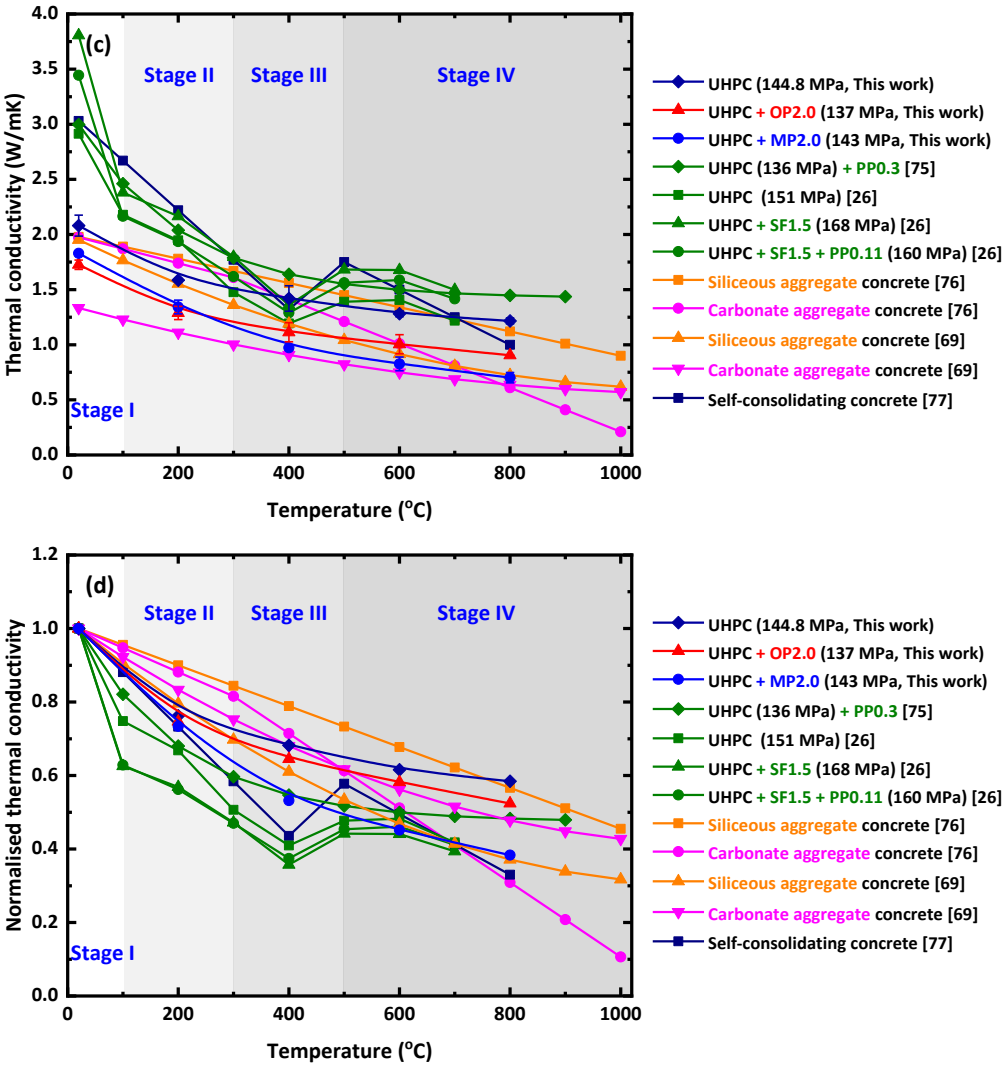


**Fig. 16.** Measured thermal conductivity of (a) SFRP fibres and (b) SFRP fibre reinforced UHPC at elevated temperatures, and (c) the thermal conductivity of normal concrete and UHPC containing hybrid fibres [26,69,75–77] and (d) the corresponding normalised form (Note: the marked strength in (c) and (d) represents the compressive strength at ambient temperature).

Fig. 16c and d show the temperature-dependent thermal conductivity of UHPC containing hybrid fibres. A similar four-stage classification of temperatures is adopted here for analysis and discussion. In Stage I, the incorporation of 2.0% OP and MP fibres can result in a 17.04% and 12.09% drop in thermal conductivity compared to that of plain UHPC. This is because polymer fibres have inherent low thermal conductivity (Fig. 16a), which is much lower than that of cement clinkers (3.35–3.45 W/m·K) and hydration products (1.25–1.32 W/m·K) [78]. Thus, the addition of SFRP fibres has a restraining effect on the thermal conductivity of UHPC as the conductivity of composite material is dependent on its constituents [79]. In addition, the thermal conductivity of plain UHPC is relatively higher than that of normal siliceous/carbonate concrete due to the denser microstructure and lower porosity of UHPC matrix [26]. In Stage II, the thermal conductivity of all UHPC specimens starts to go down initially at around 100 °C, which can be attributed to the evaporation of free water present and increase of porosity in UHPC matrix. The thermal

conductivity of pore/void (0.0259 W/m·K at 20 °C and 0.0611 W/m·K at 600 °C) is much lower than that of free water (0.683 W/m·K at 100 °C), and accordingly the loss of moisture leads to a reduction in thermal conductivity [80]. Furthermore, the melting of polymer resin in SFRP fibres takes place at around 165 °C, which would also result in a drop in thermal conductivity of SFRP fibre reinforced UHPC [75]. When the temperature is increased to over 300 °C, the loss of moisture including the remaining free water, absorbed water, and interlayer water in calcium silicate hydrate (C–S–H) leads to a steady decrease of thermal conductivity in Stage III [26]. Besides, the foaming reaction and char formation of flame retardants in SFRP fibres also lead to the increased porosity and lower thermal conductivity of UHPC matrix. The thermal conductivity of FRC-MP specimens is found to be lower than that of FRC-OP specimens under the same fibre content. This is because of the decomposition of $Mg(OH)_2$ and $Al(OH)_3$ at over 340 °C, which promotes the char formation and flame-retardant efficiency of MP fibre [59]. An abnormal increase of thermal conductivity was reported in a previous study [77], which was attributed to the dissociation of $Ca(OH)_2$ into CaO and $H_2O$ and increase of moisture at around 400 °C. In Stage IV, the loss of strongly holding moisture, together with the phase transformation of quartz from $\alpha$-type to $\beta$-type, cause a significant decrease in thermal conductivity [11,76]. Moreover, the formation of carbon-like insulation layer by SFRP fibres results in a further drop in the thermal conductivity of UHPC. The lower the thermal conductivity, the slower the temperature heating rate. Overall, the change in thermal conductivity is consistent with the temperature distribution presented and discussed in Section 4.3.

### 4.5. Microstructural evolution

#### 4.5.1. Appearance

Through splicing of confocal microscopic images, Fig. 17 illustrates the appearance of synergistic flame-retardant polymer fibre in UHPC matrix. The magnification of each sub-picture is 100 times the original size, and the overlap of image information along the edges of sub pictures makes it possible to splice. At 200 °C, there is no obvious change in the volume and shape of SFRP fibre (Fig. 17a). The melting of PP resin matrix induces some cracks along the radial direction, which can be ascribed to the high thermal expansion coefficient of PP and the shrinkage of UHPC matrix due to humidity loss [29]. With the increase of temperature to 400 °C, the shape of SFRP fibre changes a lot due to the evaporation of PP matrix at around 340 °C (Fig. 17b) [23]. The remaining volume is occupied by porous flame-retardant products, resulted from the foaming reactions among APP-PER-MEL composites and the decomposition of metallic fillers. Besides, these reactions would also generate a certain amount of inflammable gas, i.e., $NH_3$ and $CO_2$ [58], and thus the flame-retardant products are filled with macro pores. As seen in Fig. 17c, the further esterification of organic flame retardants leads to the formation of honeycomb-like structure at 600 °C, and the flame-retardant products turn into yellow colour with a slight volumetric expansion. The expansion of SFRP fibres can also cause tensile stress along the fibre-to-concrete interface and microcracks/pores may be

induced in UHPC matrix surrounding the fibre. When the temperature reaches 800 °C, the char formation and carbonization of intumescent retardant finally change the colour of SFRP fibre to black (Fig. 17d). Because of the volume expansion and inflammable gas, flame-retardant products can overflow to UHPC matrix through the connected pore structure. Moreover, SFRP fibre is closely embedded in UHPC matrix, which provides an opportunity for further exposure of flame retardants at higher temperatures. It is noted that the physical and chemical variations of SFRP fibres are highly related to the thermal and mechanical properties of UHPC matrix.

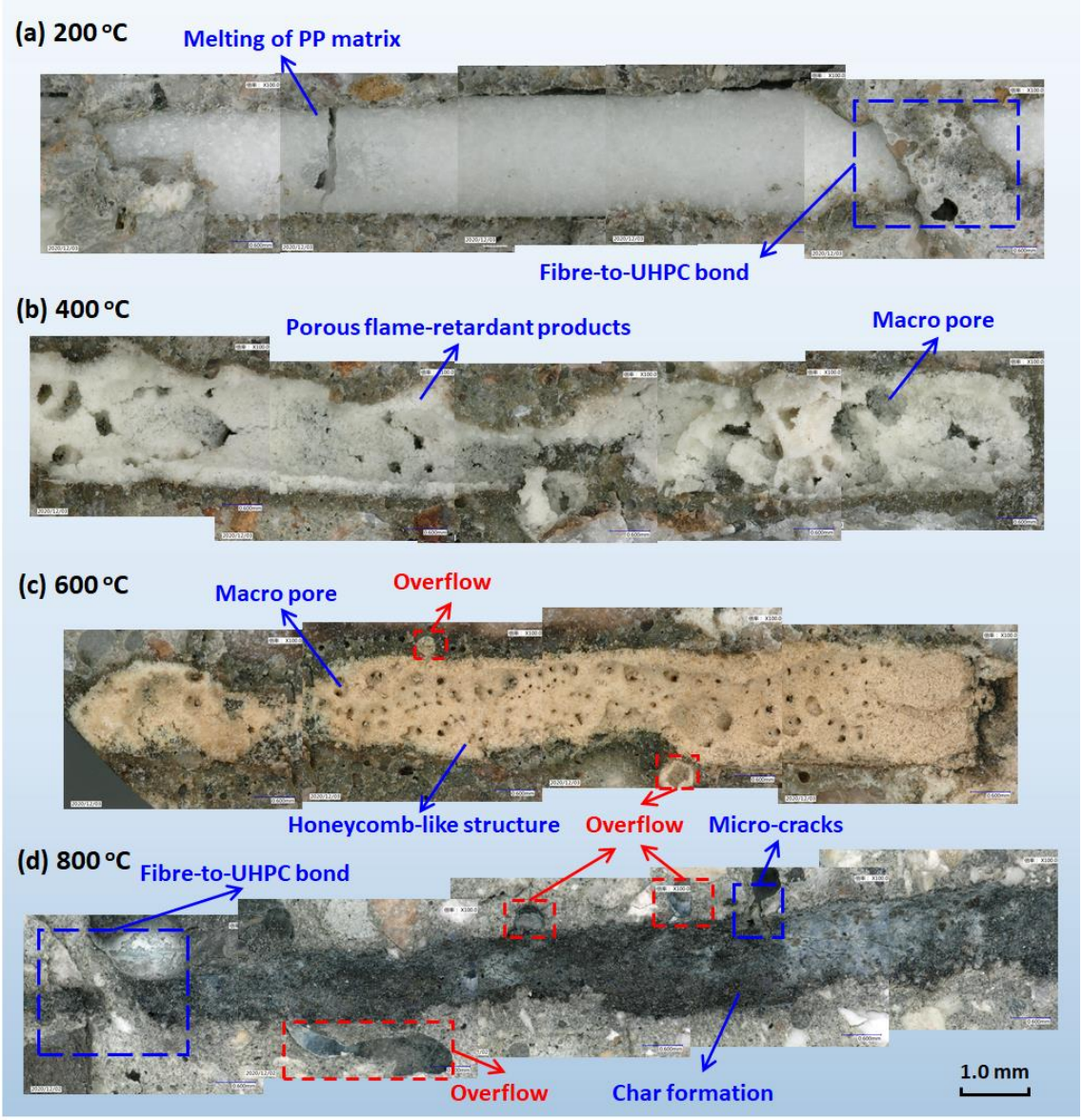


**Fig. 17.** 3D confocal microscopic images of FRC-MP02 at elevated temperatures.

4.5.2. Element map

The distribution of five main elements including Si, O, Ca, Al, and Mg in plain UHPC and FRC specimens after heat exposure is displayed with two-dimensional colour maps in Fig. 18. Each colour represents a different element content as determined using EPMA method. For non-metallic elements, the Si and O elemental concentrations can be mainly explained by the presence of $SiO_2$ in

cement clinkers, hydration products, and fine aggregates. The incorporation of SFRP fibres has no obvious influence on the distribution of these two elements. For metallic elements, the elemental concentration of Ca is the highest due to the existence of C–S–H, CH, and CaO, especially in plain UHPC sample. In contrast, the Al and Mg elemental concentrations are relatively low (Fig. 18a), which can be ascribed to the small amount of $Al_2O_3$ and MgO decomposed by carbonate phases. As seen in Fig. 18b and c, there exists an abnormal distribution of Al and Mg. The high elemental concentration of Al in the left part of the map for FRC-OP02 can be explained by the presence of fine aggregate, which is mainly composed of $Al_2O_3$ and $SiO_2$, as introduced in Section 2.1. The scattered distribution of Al and Mg elements in the maps for FRC-MP02 can be ascribed to the overflow of flame-retardant products, consisting of $Mg(OH)_2$ and $Al(OH)_3$ as well as their decomposed products, induced by the foaming reactions and volume expansion of SFRP fibres.

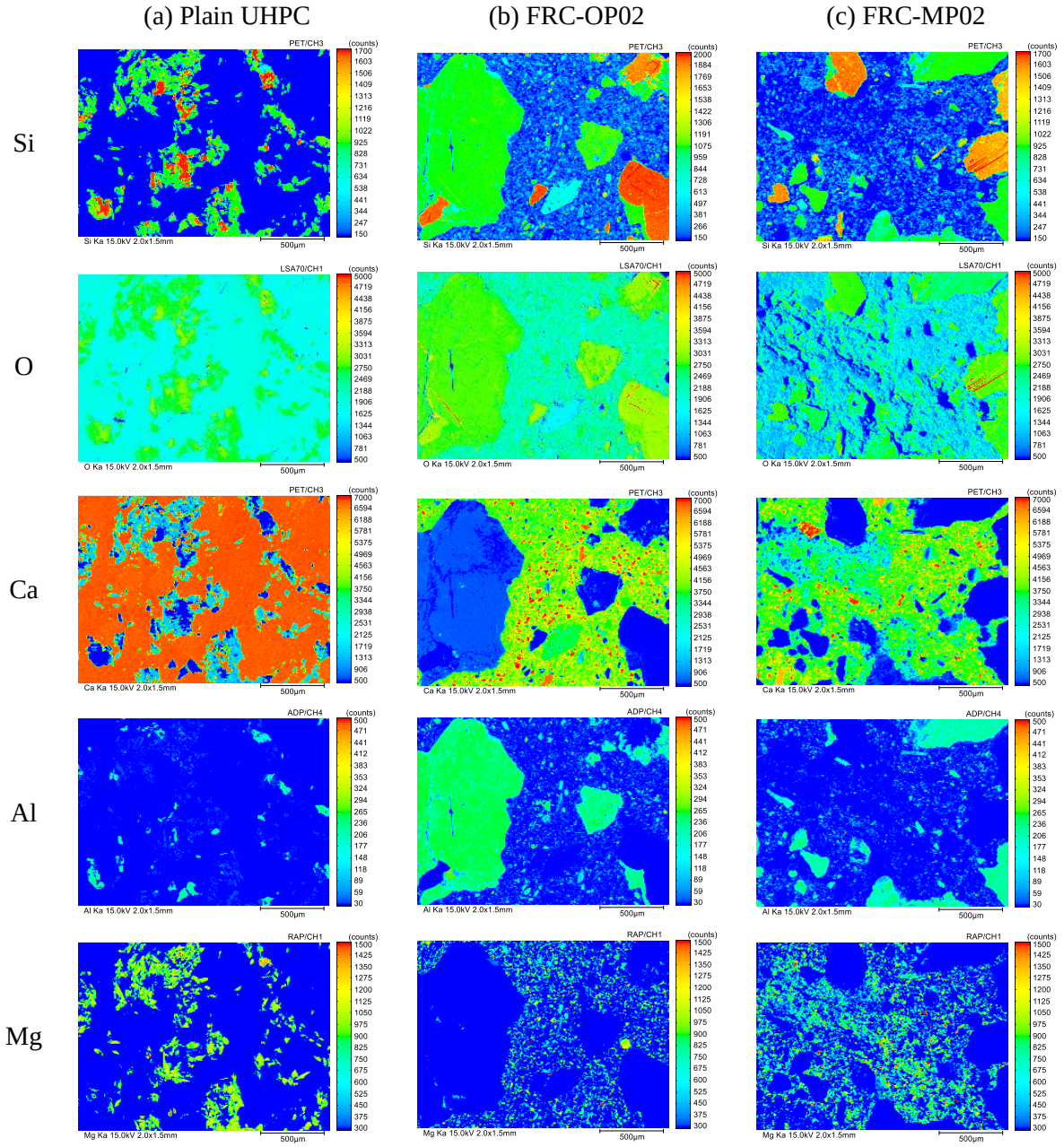


**Fig. 18.** Elemental maps of plain UHPC and FRC specimens after heat exposure.

4.5.3. Pore structure

Fig. 19 shows the pore size distribution of UHPC specimens with/without SFRP fibres at elevated temperatures. The pore size with the highest incremental intrusion volume is defined as the critical radius for creating a connected path [49]. As seen in Fig. 19a, the critical radius of all UHPC specimens lies around 74.5 nm at 200 °C. With the temperature reaching 600 °C, the critical radius of plain UHPC decreases to only 60.0 nm, while that of FRC-OP02 and FRC-MP02 increase to 92.0 and 113.8 nm, respectively, in Fig. 19b. This suggests that the addition of SFRP fibres promotes the connectivity of larger pores in UHPC matrix at elevated temperatures. At 200 °C, the incorporation of 2.0% OP and MP fibres can lead to a 79.21% and 114.16% increase of porosity, respectively, compared with plain UHPC as displayed in Fig. 19c. The porosity of all specimens increases when the temperature increases to 600 °C, while the relative relationship of porosity among tested specimens maintains and the highest porosity is still found in FRC-MP02 (Fig. 19d). The pore size at 50% cumulative intrusion volume is referred to as the median pore radius [81]. The median pore radius of plain UHPC decreases from 83.3 to 74.5 nm with the increase of temperature from 200 to 600 °C, suggesting the poorer permeability of pore structure. In contrast, the median pore radius of FRC-OP02 and FRC-MP02 has a 23.83% and 39.64% increase, respectively, over the measured temperature range. The promoted permeability induced by foaming reactions of flame retardants in SFRP fibres is helpful to prevent explosive spalling of UHPC [10,25], and MP fibre performs better than OP fibre in terms of permeability enhancement.

To gain more insights into the evolution of pore structure, the pore distribution is grouped into five scale ranges: gel pores (<10 nm), meso pores (10–100 nm), middle capillary pores (100–1000 nm), large capillary pores (1–10 μm), and macro pores (>10 μm) [82], as illustrated in Fig. 19e and f. The dominant pore range of plain UHPC is meso pores, which represents over half of the pore volume fraction at both 200 and 600 °C. The volume fraction of middle capillary pores decreases from 18% to 12%, while that of macro pores increases significantly from 14% to 22% with the increase of temperature from 200 to 600 °C. For FRC specimens, although meso pores are still the dominant pore range, macro pores become the second-highest one representing approximately double pore volume than that of plain UHPC at 200 °C. The increase in macro pores is attributed to the ITZ between SFRP fibres and UHPC matrix, as well as the additional zones induced by the melting of polymer resin in fibres [29]. At 600 °C, the volume of middle capillary pores in FRC specimens increases dramatically to nearly triple that of 200 °C, and middle capillary even pores become the dominant pore range in FRC-MP02 which represents 37% pore fraction. This is attributed to the foaming reactions of organic and metallic flame retardants in SFRP fibres, creating more connected paths of middle capillary pores. The increase of temperature and incorporation of SFRP fibres have insignificant effect on gel pores and large capillary pores.

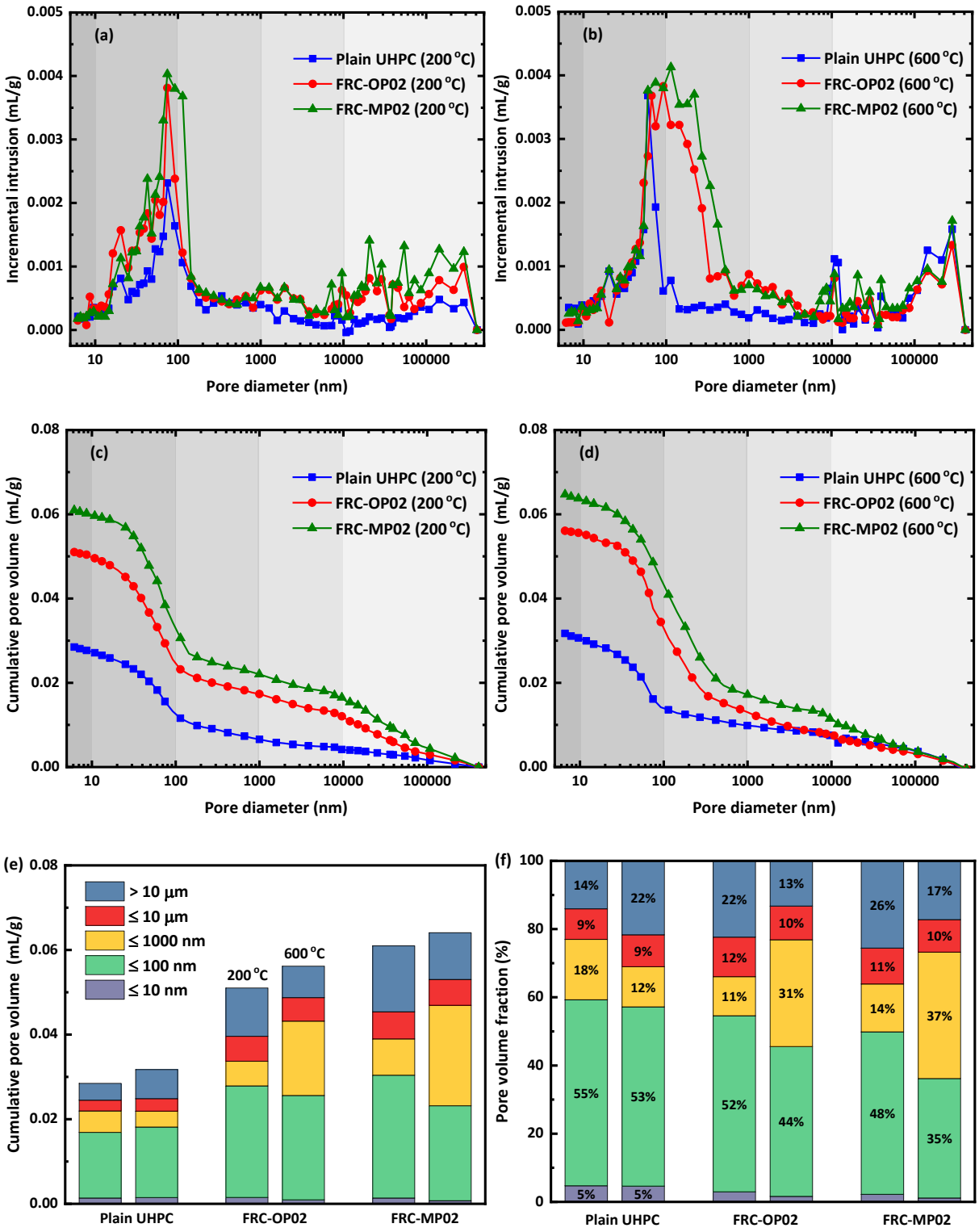


**Fig. 19.** (a)–(d) Pore size distribution of UHPC specimens after exposure to 200 and 600 °C, and (e) cumulative pore volume and (f) pore volume friction under five-scale pore size classification.

### 4.6. Micromechanical properties

Fig. 20 presents the load-displacement curves of individual phases from nanoindentation tests and the corresponding SEM images of residual indent impression. The variation of load-displacement curves is associated with the dimension of residual indent. The lower the displacement of the curve and the smaller the dimension of indent impression, the higher the properties (e.g., elastic modulus

and hardness) of individual phases. It is worth noting that even the same phase can exhibit different micromechanical properties due to the heterogeneity of cement hydration [50]. Based on the difference in elastic modulus and hardness, the phases in UHPC specimens can be divided into three categories, namely low-density (LD), high-density (HD), and ultra-high-density (UHD) phases. The former two types represent C–S–H and CH phases, while the last type of phase is referred to as the fine aggregate [12,83].

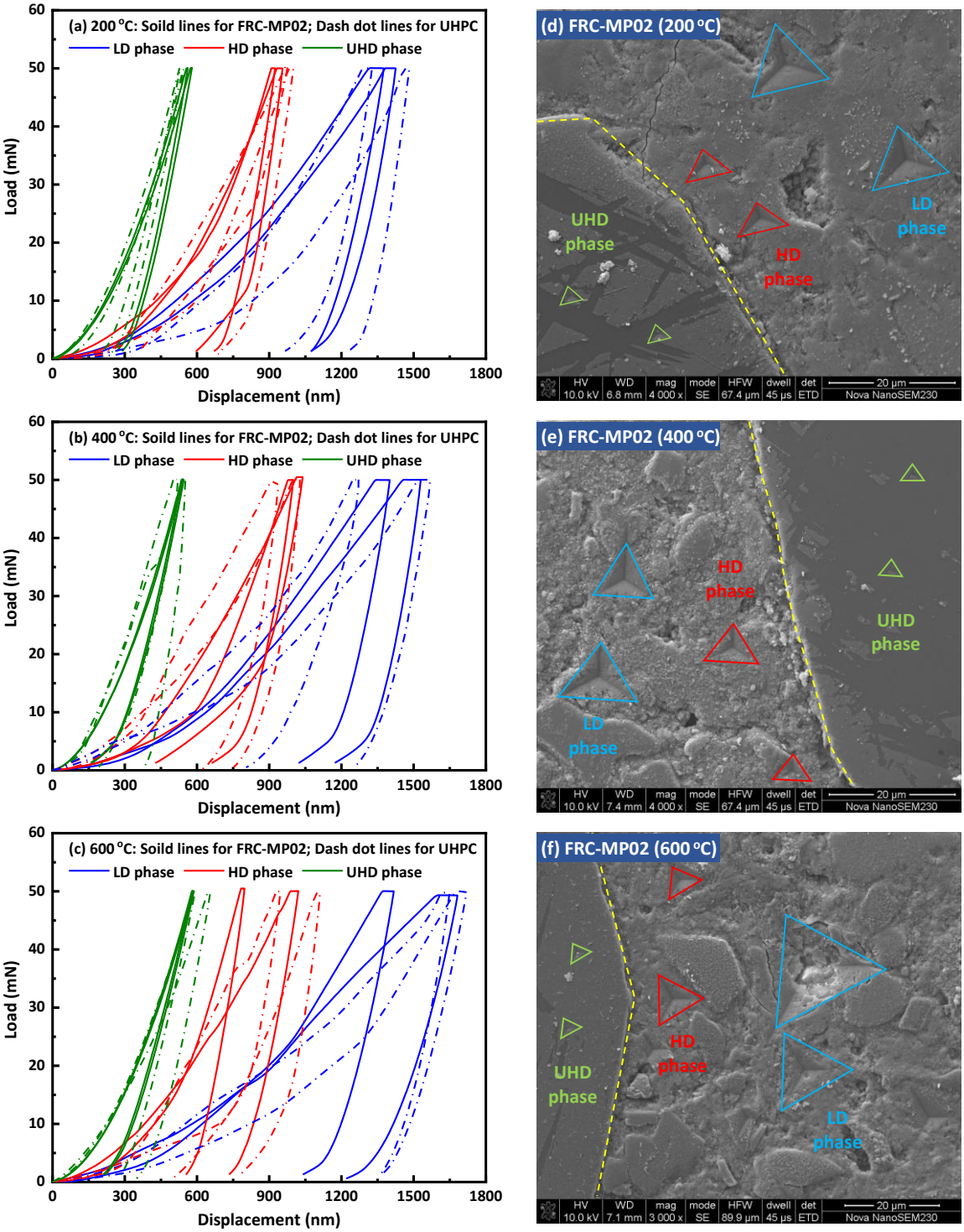


**Fig. 20.** Load-displacement curves of different phases measured by nanoindentation test, and the corresponding SEM images of residual indent impression of FCR-MP02.

The displacement of UHD phases is generally lower than that of LD and HD phases, while the slope of the load-displacement curve for UHD phases is higher than that of LD and HD phases (Fig. 20a–c). This implies that the UHD phases have the highest elastic modulus and hardness, followed by HD and LD phases. As seen in Fig. 20a, there is a slight difference in the displacement of each type of phase between plain UHPC and FRC-MP02 at 200 °C. Fig. 20b indicates that the slopes of loading portion of all curves decrease, suggesting the decrease in elastic modulus of all phases at 400 °C [12]. In particular, the displacement of LD phases in plain UHPC fluctuates the most from 1147 to 1568 nm. When the temperature rises to 600 °C, the load-displacement curves slant to right with the further decrease of loading slopes (Fig. 20c), indicating the further decrease of elastic properties. In addition, the decrease in slope of load-displacement curves is even more obvious for plain UHPC than that for FRC-MP02, implying the relatively lower elastic modulus of plain UHPC. Therefore, the incorporation of SFRP fibres has a restraining effect on the reduction in elastic modulus of individual phases at elevated temperatures, leading to a positive effect on residual compressive strength of UHPC, as discussed in Section 4.2.

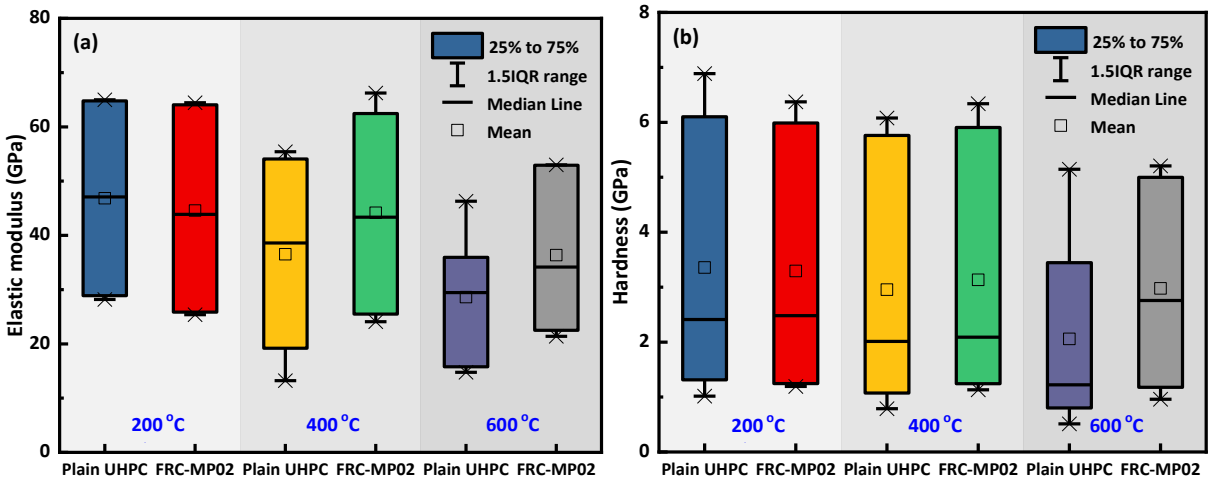


**Fig. 21.** Statistical analysis of (a) elastic modulus and (b) hardness of individual phases in plain UHPC and FRC-MP02 at elevated temperatures.

Fig. 21 presents a statistical analysis of elastic modulus and hardness of individual phases based on the nanoindentation test results. At 200 °C, the elastic modulus of material phases in plain UHPC is fluctuant between 28.19 and 64.99 GPa (Fig. 21a), corresponding to the LD phases and UHD phases, respectively. Nevertheless, the mean elastic modulus of plain UHPC decreases significantly from 46.83 to 36.52 GPa with the increasing temperature from 200 to 400 °C, and further drops to only 28.62 GPa at 600 °C. The mean elastic modulus of FRC-MP02 is 4.80% lower than that of plain UHPC at 200 °C but becomes 20.92% and 27.04% higher than that of plain UHPC at 400 and 600 °C, respectively. Regarding the hardness, LD phases and UHD phases of plain UHPC also lead to the upper and lower boundaries of hardness. The mean hardness of plain UHPC decreases from 3.35 to 2.59 GPa with the increase of temperature from 200 to 400 °C, and further drops significantly to only 2.06 GPa at 600 °C. As seen in Fig. 21b, FRC-MP02 has a higher

hardness than plain UHPC over the measured temperature range. It should be mentioned that although the mean values of mechanical properties obtained from nanoindentation tests may not fully represent the effective properties of UHPC due to the limitation of sample number [50,83], the similar change trends of load-displacement curves and measured elastic properties suggest that FRC-MP02 has better micromechanical properties than plain UHPC at elevated temperatures.

## 5. Discussion

### 5.1. Mechanism for thermal damage of plain UHPC

Fig. 22 illustrates the mechanism for thermal damage of plain UHPC at elevated temperatures. In consistence with Section 4, the four-stage division of temperature is employed for the following discussion, with a special focus on 100, 300 and 500 $^{o}$C as three key temperature points.

(i) At Stage I, the gradual evaporation of free water leads to approximately 2% mass loss (Fig. 10), while the hydrothermal reactions of cement clinkers result in a slight increase in compressive strength (Fig. 13) [72]. Besides, the increase in porosity and permeability induces a significant drop of about 12% in the thermal conductivity of UHPC matrix (Fig. 16).

(ii) At Stage II, the leftover free water evaporates intensively at around 105 $^{o}$C, along with the loss of physically absorbed water starting at over 100 $^{o}$C. Fig. 22a displays the presence of free water in capillary pores as well as the absorbed water and bound water within C–S–H gels [84]. The evaporation of water directly causes an obvious loss of mass (Fig. 10) and a significant increase in porosity, leading to a gradual decrease in thermal conductivity with increasing temperature from 100 to 300 $^{o}$C (Fig. 16). However, the dense microstructure in UHPC matrix slows down the evaporation of moisture content, and accordingly, only less than 25% of the total mass loss occurs over this stage compared with that of 70% in normal concrete [61]. The increase of surface forces due to water removal and the build-up pore pressure results in an abnormal increase of around 5% in compressive strength of UHPC at around 200 $^{o}$C (Fig. 13) [63].

(iii) At Stage III, the loss of adsorbed water and chemically bound water in the interlayers of C–S–H gels takes place (Fig. 22b), which leads to a further drop in mass and thermal conductivity. Besides, calcium hydroxide starts to dissociate into CaO and $H_2O$ at around 375 $^{o}$C and the continuous decomposition of C–S–H gels throughout this stage [16], resulting in a dramatic decrease up to 45% in compressive strength (Fig. 13). In addition, the rapid evaporation of absorbed, bound, and decomposed water would lead to a high pore pressure in UHPC matrix [4].

(iv) When the temperature reaches over 500 $^{o}$C, quartz phase transformation occurs in fine aggregates, and the thermal incompatibility between aggregates and UHPC matrix would induce microcracks and voids [11], as illustrated in Fig. 22(c). In Stage IV, the variations of mass loss and thermal conductivity continue, as similar to that in Stage III, but with a smaller evolution (Figs. 10 and 16) due to the limited amount of chemically bound water remaining [26]. The continuous decomposition of CH and C–S–H gels lasts until 600 and 860 $^{o}$C [85], respectively, which would

cause the reduction in elastic modulus and hardness of individual phases (Fig. 20), as well as the decrease in compressive strength to only around 20% of the original strength (Fig. 13).

Coupled with these physicochemical changes, the transport of moisture and vapour would also lead to the thermal damage of UHPC at elevated temperatures. Based on the MIP measurement, meso pores ranging smaller than 100 nm is the dominant pore range (Fig. 19), and the porosity of plain UHPC is much lower than that of normal concrete [2]. The dense microstructure may hinder the migration of moisture, and accordingly, plain UHPC is vulnerable to pore pressure-induced stress [23]. In addition, the temperature gradient raised by high heating rate (Fig. 15) would generate excessive thermal stress in UHPC matrix [10]. The combined effects of pore pressure and thermal stress can induce explosive spalling (Fig. 11), which not only affects the structural integrity but also intensifies the thermal damage and accelerates the heat transfer towards internal matrix [14].

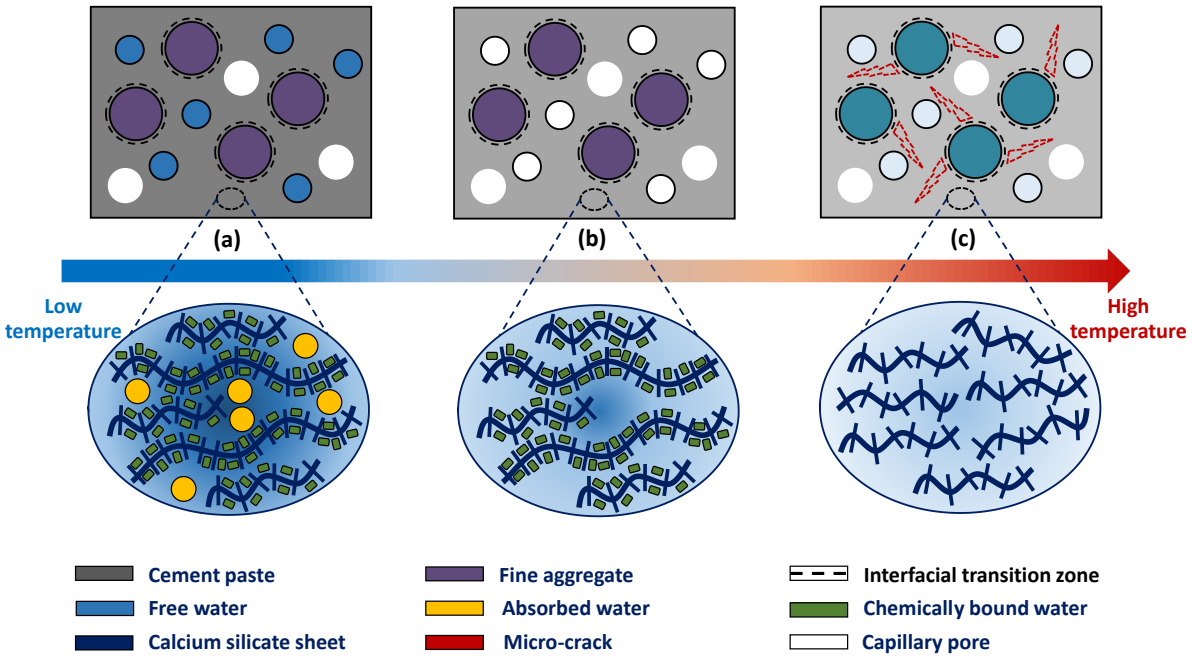


**Fig. 22.** Illustration of the mechanism for thermal damage of plain UHPC at elevated temperatures (Note: the lighter the colour, the more the loss of moisture).

### 5.2. Mechanism for thermal damage mitigation by synthetic flame-retardant polymer fibres

The mechanism for mitigating high temperature-induced damage of UHPC is closely associated with physical and chemical changes of SFRP fibres, including melting, foaming, overflowing, and char formation, as illustrated in Fig. 23, which can also be explained with four temperature stages.

(i) At Stage I, the addition of SFRP fibres does not influence the hydration process of UHPC [33,61]. SFRP fibres are well embedded in UHPC matrix (Fig. 23a) as confirmed by macroscopic and microscopic images in Figs. 11 and 17. Although the low-modulus polymer fibres would lead to a drop in compressive strength and elastic modulus of UHPC [86], the strength loss caused by SFRP fibres is inferior to commonly used PP and PVA fibres under the same fibre content (Fig. 13). As revealed by AFM analysis, the addition of high-modulus metallic fillers promotes the adhesion and

elastic modulus of MP fibre (Fig. 9), which consequently improve the compressive behaviour of UHPC and FRC-MP01 even has higher compressive strength than that of plain UHPC. Moreover, the thermal conductivity of SFRP fibres is less than a quarter to that of UHPC matrix, resulting in a lower thermal conductivity of FRC compared to plain UHPC (Fig. 16).

(ii) At stage II, SFRP fibres starts to melt at around 165 °C as seen in TG curves (Fig. 7) which is similar to the melting point of PP resin matrix. The MIP results reveal that the incorporation of SFRP fibres would enhance the porosity of UHPC matrix and promote the volume fraction of larger pores sizing over 10 μm (Fig. 13), which can be attributed to the additional ITZ between fibres and UHPC matrix as well as the left gaps by fibre melting [10]. The thermal expansion coefficient of PP resin is 10 times higher than that of UHPC matrix, and thus the thermal mismatch between SFRP fibres and UHPC matrix would induce microcracks along the radial direction of fibres [23]. Accordingly, the enhanced pore structure of UHPC matrix by SFRP fibres provides more channels for water evaporation and heat exchange, and also leads to an increase in mass loss (Fig. 10) and decrease in thermal conductivity (Fig. 16).

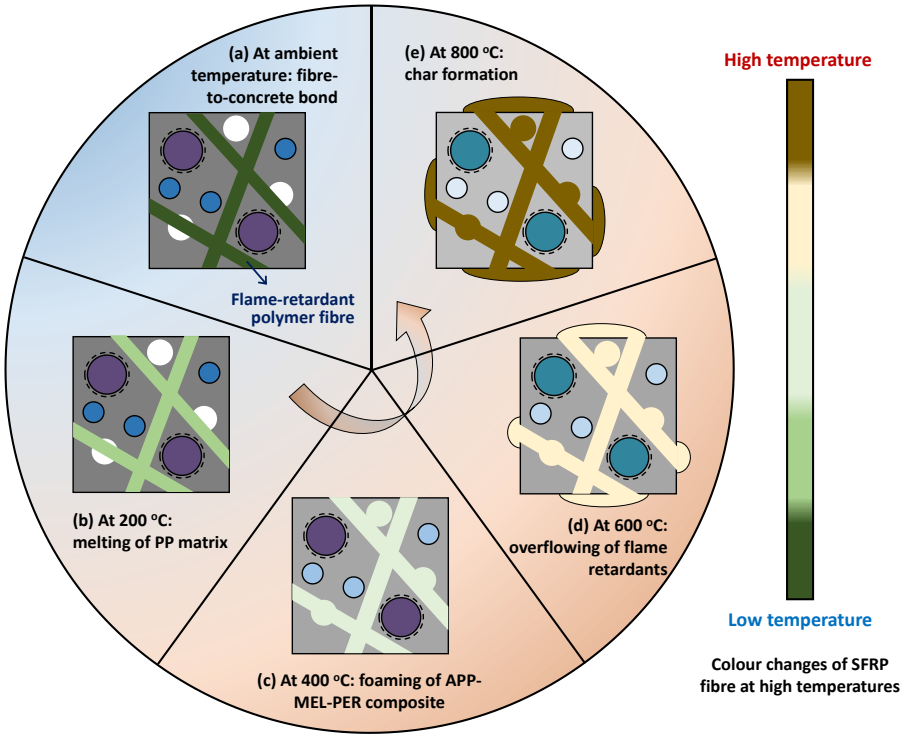


**Fig. 23.** Illustration of the mechanism for mitigating thermal damage by SFRP fibres.

(iii) At Stage III, the commonly used polymer fibres might lose their effectiveness due to the evaporation of polymer resin at over 340 °C [25]. In contrast, the intensive foaming reactions of metallic-organic flame retardants in SFRP fibres can still help further mitigate the thermal damage of UHPC over this stage. Following the TG, DSC, and FTIR analyses, the potential chemical reactions are as illustrated in Fig. 24. The first series of reactions include the decomposition of ammonium polyphosphate at around 250 °C, and the resulting phosphoric acid triggers the dehydration and esterification of carbon sources [56], i.e., reactions (a)–(c). When the temperature

increases to 300 °C, nitrogen sources begins to dehydrate, forming an extended structure and releasing non-flammable gase [58]. The further esterification and endothermic reactions among flame retardants, i.e., reactions (d)–(f), lead to the formation of honeycomb-like char (Fig. 17). It is noted that the decomposition and foaming interactions of organic flame retardants occur in the same temperature range of 300–480 °C (Fig. 8), which promotes the esterification among flame retardants and facilitate the formation of insulation layer [56]. Additionally, the decompositions of metallic fillers into metallic oxides, i.e., reactions (g)–(j), would also have a promoting effect on the formation of insulation char [52].

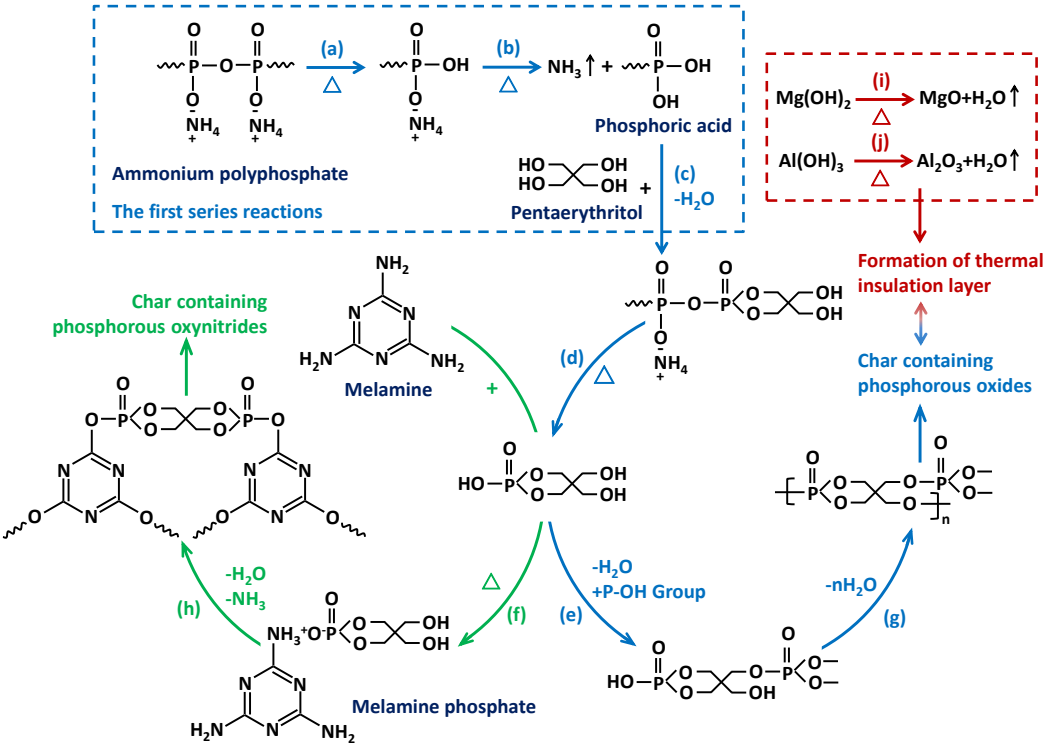


**Fig. 24.** Schemes of the foaming reactions of synergistic flame-retardant polymer fibres.

At this stage, the mechanism for mitigating thermal damage by SFRP fibres can be explained from three aspects. Firstly, the foaming reactions among intumescent flame retardants further enhance the connectivity of pore structure in UHPC matrix. As seen in pore size distribution, both the porosity and volume fraction of larger pores, especially the middle capillary pores, increase significantly by adding SFRP fibres, resulting in the higher mass loss (Fig. 10) and lower thermal conductivity (Fig. 16) compared to that of plain UHPC. Besides, different from the commonly-used polymer fibres, the left space by SFRP fibres is filled with honeycomb-like insulation char rather than the void/air at Stage III (Fig. 17). As illustrated in Fig. 23(c), porous flame-retardant products can fill the thermal stress-induced pores/cracks driven by the non-flammable gas and extended char. The filling effect of flame-retardant products helps slow down the heating rate of UHPC matrix under one-side heating, which contributes to the improvement of fire resistance for composite slabs (Fig. 15). Finally, the degradation of elastic modulus and hardness of individual phases in UHPC is

slowed down as confirmed by the nanoindentation test (Fig. 20), and accordingly the compressive strength loss of FRC is much lower than that of plain UHPC over this temperature range (Fig. 12).

(iv) At Stage IV, the carbonization of honeycomb-like structure leads to the colour change of SFRP fibres from white to yellow, which finally turns to black (Fig. 17). Driven by the volume expansion of fibres, the intumescent flame-retardant products can fill the macro pores of UHPC matrix (Fig. 18), overflow to the surface of structures (Fig. 11), and even form a local insulation layer over the heating surface as illustrated in Fig. 23d and e. Regarding the pore structure, the volume fraction of middle and large capillary pores increases intensively, leading to an increased in total pore volume. The pore structure follows a similar change trend to mass loss and thermal conductivity in Stage III. Regarding the mechanical properties, although the elastic modulus and hardness of individual phases in FRC-MP02 decrease with temperature as indicated by nanoindentation tests, the degradation degree is inferior to plain UHPC over this stage (Fig. 21). Accordingly, the compressive strength of FRC specimens is much higher than that of plain UHPC (Fig. 12), and the failure mode under compression also suggests that the softening of UHPC matrix is restrained by incorporating SFRP fibres.

## 6. Conclusions

In this study, two types of synergistic flame-retardant polymer (SFRP) fibres were developed. A series of tests were carried out to investigate the chemical properties of them and the effectiveness of them on mitigating the damage of ultra-high performance concrete (UHPC) at elevated temperatures. Based on the experimental results, the main conclusions can be drawn as follows:

- The SFRP fibres experience complex physical and chemical processes, including melting, foaming, overflowing and carbonization. The char formation of SFRP fibres is dominated by the esterification and endothermic reactions among organic flame retardants, including ammonium polyphosphate, pentaerythritol, and melamine over the temperature range of 161–491 $^{o}$C. Besides, the incorporation of metallic fillers, i.e., $Mg(OH)_2$ and $Al(OH)_3$, can improve the thermal stability (e.g., lower heat release rate but higher decomposed temperature), and promote the micro-mechanical properties (i.e., adhesion and elastic modulus) of SFRP fibres.
- At ambient temperature, the incorporation of 1.0 vol% modified polymer (MP) fibre would cause a 1.45% strength increase of UHPC. Although a 1.54% strength loss occurs when the volume fraction of MP fibre increases to 2.0%, the negative effect on compressive behaviour of UHPC is inferior to commonly used polymer fibres, e.g., PP and PVA fibres, under the same fibre content.
- At elevated temperatures, the residual elastic modulus of UHPC reinforced with 2.0% organic polymer (OP) fibre is 24.3% (400 $^{o}$C) and 114.8% (600 $^{o}$C) higher than that of plain UHPC. Besides, MP fibre performs better than OP fibre in terms of promoting the temperature-dependent compressive strength of UHPC. Although SFRP fibres have insignificant effect on

the failure mode of UHPC under uniaxial compression, the shear sliding along the X-shaped shear plane can be restrained by fibres and FRC specimens have better integrity after the compressive failure.

- The incorporation of SFRP fibres can help reduce the temperature increasing rate and prolong the time to reach the fire-resistant limit of UHPC slabs under one-side heating condition. SFRP fibre reinforced UHPC specimens have lower thermal conductivity than plain UHPC, which can be ascribed to the low thermal conductivity of SFRP fibres and the thermal mismatch between SFRP fibres and UHPC matrix at elevated temperatures. The incorporation of 2.0% MP fibre is suggested considering the thermal performance and efficiency of SFRP fibres in mitigating the thermal-induced damage of UHPC.
- The multi-physical and chemical reactions of SFRP fibres including phase transformation of PP resin and foaming reactions of metallic-organic flame retardants result in an enhanced pore connectivity in UHPC matrix. Consequently, more thermal exchange channels, especially the middle and large capillary pores, are available for the rapid evaporation of free, absorbed and bound water, which helps prevent the explosive spalling of UHPC.
- Driven by non-flammable gas and volume expansion, flame-retardant products can fill the thermal stress-induced pores/cracks, and even overflow to the heating surface forming a local insulation layer. Accordingly, the heating rate of UHPC matrix is slowed down, resulting in a reduced temperature gradient within the composite slabs.
- The degradation of micromechanical properties (i.e., elastic modulus and hardness) of LD, HD, and UHD phases with temperature is delayed in UHPC reinforced with SFRP fibres due to the slower decomposition rate of hydrated products in UHPC matrix associated with the slower temperature rising rate.

To sum up, the experimental investigation on behaviour of SFRP fibre reinforced UHPC at elevated temperatures indicates that SFRP fibres can help effectively mitigate the thermal damage of UHPC subjected to high temperatures. In this study, only the thermal and compressive behaviour and microstructural evolution were investigated to gain insights into the damage evolution and mitigation mechanism. Towards practical applications, the effects of SFRP and hybrid fibres on static and dynamic mechanical properties of UHPC at elevated temperatures need to be explored [87–89], which is the subject of ongoing research and will be presented in future publications.

**Acknowledgements**

The authors greatly acknowledge the financial support from the National Natural Science Foundation of China (52078378), National Key Research and Development Program of China (2018YFB2101000), Research Program of State Key Laboratory of Disaster Reduction in Civil Engineering, and Fundamental Research Funds for the Central Universities. The financial support provided by China Scholarship Council (CSC) to the first author is also gratefully acknowledged.

**References**


[1] X. Ouyang, C. Shi, Z. Wu, K. Li, B. Shan, J. Shi, Experimental investigation and prediction of elastic modulus of ultra-high performance concrete (UHPC) based on its composition, Cem. Concr. Res. 138 (2020) 106241.

[2] D. Wang, C. Shi, Z. Wu, J. Xiao, Z. Huang, Z. Fang, A review on ultra high performance concrete: Part II. Hydration, microstructure and properties, Constr. Build. Mater. 96 (2015) 368–377.

[3] Y. Li, Y. Zhang, E.H. Yang, K.H. Tan, Effects of geometry and fraction of polypropylene fibers on permeability of ultra-high performance concrete after heat exposure, Cem. Concr. Res. 116 (2019) 168–178.

[4] Y. Zhu, H. Hussein, A. Kumar, G. Chen, A review: Material and structural properties of UHPC at elevated temperatures or fire conditions, Cem. Concr. Compos. 123 (2021) 104212.

[5] Q. Ma, R. Guo, Z. Zhao, Z. Lin, K. He, Mechanical properties of concrete at high temperature-A review, Constr. Build. Mater. 93 (2015) 371–383.

[6] H. Wu, X. Lin, A. Zhou, A review of mechanical properties of fibre reinforced concrete at elevated temperatures, Cem. Concr. Res. 135 (2020) 106117.

[7] Z. Yan, Y. Shen, H. Zhu, X. Li, Y. Lu, Experimental investigation of reinforced concrete and hybrid fibre reinforced concrete shield tunnel segments subjected to elevated temperature, Fire Saf. J. 71 (2015) 86–99.

[8] Y. Zhang, Y. Shen, R. Carvel, H. Zhu, Y. Zhang, Z. Yan, Experimental investigation on the evacuation performance of pedestrians in a three-lane urban tunnel with natural ventilation in a fire scenario, Tunn. Undergr. Sp. Technol. 108 (2021) 103634.

[9] C. Guo, Q. Guo, T. Zhang, W. Li, H. Zhu, Z. Yan, Study on real-time heat release rate inversion for dynamic reconstruction and visualization of tunnel fire scenarios, Tunn. Undergr. Sp. Technol. 122 (2022) 104333.

[10] M. Zeiml, D. Leithner, R. Lackner, H.A. Mang, How do polypropylene fibers improve the spalling behavior of in-situ concrete, Cem. Concr. Res. 36 (2006) 929–942.

[11] G.A. Khoury, Effect of fire on concrete and concrete structures, Prog. Struct. Eng. Mater. 2 (2000) 429–447.

[12] M.J. DeJong, F.J. Ulm, The nanogranular behavior of C-S-H at elevated temperatures (up to 700 $^{o}$C), Cem. Concr. Res. 37 (2007) 1–12.

[13] Z. Jia, C. Chen, J. Shi, Y. Zhang, Z. Sun, P. Zhang, The microstructural change of C-S-H at elevated temperature in Portland cement/GGBFS blended system, Cem. Concr. Res. 123 (2019) 105773.

[14] L. Shen, F. Lo Monte, G. Di Luzio, G. Cusatis, W. Li, R. Felicetti, F. Lombardi, M. Lualdi, M. Cao, Q. Ren, On the moisture migration of concrete subject to high temperature with different heating rates, Cem. Concr. Res. 146 (2021) 106492.

[15] C. Jiang, J. Fang, J.Y. Chen, X.L. Gu, Modeling the instantaneous phase composition of cement pastes under elevated temperatures, Cem. Concr. Res. 130 (2020) 105987.

[16] T. Zhang, H. Zhu, L. Zhou, Z. Yan, Multi-level micromechanical analysis of elastic properties

of ultra-high performance concrete at high temperatures : Effects of imperfect interface and inclusion size, Compos. Struct. 262 (2021) 113548.

[17] D. Stefaniuk, L. Sadowski, M. Javad, A. Qomi, Engineering of high specific strength and low thermal conductivity cementitious composites with hollow glass microspheres for high-temperature high-pressure applications, Cem. Concr. Compos. (2020) 103514.

[18] Z. Shen, H. Zhou, A. Brooks, D. Hanna, Evolution of elastic and thermal properties of cementitious composites containing micro-size lightweight fillers after exposure to elevated temperature, Cem. Concr. Compos. 118 (2021) 103931.

[19] X. Jiang, R. Xiao, Y. Bai, B. Huang, Y. Ma, Influence of waste glass powder as a supplementary cementitious material (SCM) on physical and mechanical properties of cement paste under high temperatures, J. Clean. Prod. 340 (2022) 130778.

[20] A. Ricklefs, A.M. Thiele, G. Falzone, G. Sant, L. Pilon, Thermal conductivity of cementitious composites containing microencapsulated phase change materials, Int. J. Heat Mass Transf. 104 (2017) 71–82.

[21] A. Jayalath, L. Aye, T. Ngo, P. Mendis, Multi-scale analysis on thermal properties of cement-based materials containing micro-encapsulated phase change materials, Constr. Build. Mater. 254 (2020) 119221.

[22] Z. Huang, K. Padmaja, S. Li, J.Y.R. Liew, Mechanical properties and microstructure of ultra-lightweight cement composites with fly ash cenospheres after exposure to high temperatures, Constr. Build. Mater. 164 (2018) 760–774.

[23] Y. Li, K.H. Tan, E.H. Yang, Synergistic effects of hybrid polypropylene and steel fibers on explosive spalling prevention of ultra-high performance concrete at elevated temperature, Cem. Concr. Compos. 96 (2019) 174–181.

[24] J.D. Ríos, H. Cifuentes, C. Leiva, S. Seitl, Analysis of the mechanical and fracture behavior of heated ultra-high-performance fiber-reinforced concrete by X-ray computed tomography, Cem. Concr. Res. 119 (2019) 77–88.

[25] D. Zhang, K.H. Tan, Effect of various polymer fibers on spalling mitigation of ultra-high performance concrete at high temperature, Cem. Concr. Compos. 114 (2020) 103815.

[26] V. Kodur, S. Banerji, R. Solhmirzaei, Effect of Temperature on Thermal Properties of Ultrahigh-Performance Concrete, J. Mater. Civ. Eng. 32 (2020) 04020210.

[27] J.J. Park, D.Y. Yoo, S. Kim, S.W. Kim, Benefits of synthetic fibers on the residual mechanical performance of UHPFRC after exposure to ISO standard fire, Cem. Concr. Compos. 104 (2019) 103401.

[28] G. Mazzucco, C.E. Majorana, V.A. Salomoni, Numerical simulation of polypropylene fibres in concrete materials under fire conditions, Comput. Struct. 154 (2015) 17–28.

[29] G.A. Khoury, Polypropylene fibres in heated concrete Part 2: Pressure relief mechanisms and modelling criteria, Mag. Concr. Res. 9831 (2008) 189–204.

[30] D. Suescum-Morales, J.D. Ríos, A.M. De La Concha, H. Cifuentes, J.R. Jiménez, J.M. Fernández, Effect of moderate temperatures on compressive strength of ultra-high-performance concrete: A microstructural analysis, Cem. Concr. Res. 140 (2021) 106303.

[31] M. Ozawa, H. Morimoto, Effects of various fibres on high-temperature spalling in high-performance concrete, Constr. Build. Mater. 71 (2014) 83–92.

[32] D. Zhang, K.H. Tan, A. Dasari, Y. Weng, Effect of natural fibers on thermal spalling resistance of ultra-high performance concrete, Cem. Concr. Compos. 109 (2020) 103512.

[33] T. Zhang, Y. Zhang, Z. Xiao, Z. Yang, H. Zhu, J.W.W. Ju, Z. Yan, Development of a novel bio-inspired cement-based composite material to improve the fire resistance of engineering structures, Constr. Build. Mater. 225 (2019) 99–111.

[34] J. Gu, G. Zhang, S. Dong, Q. Zhang, J. Kong, Study on preparation and fire-retardant mechanism analysis of intumescent flame-retardant coatings, Surf. Coatings Technol. 201 (2007) 7835–7841.

[35] S. Zhou, L. Song, Z. Wang, Y. Hu, W. Xing, Flame retardation and char formation mechanism of intumescent flame retarded polypropylene composites containing melamine phosphate and pentaerythritol phosphate, Polym. Degrad. Stab. 93 (2008) 1799–1806.

[36] J.Z. Liang, J.Q. Feng, C.P. Tsui, C.Y. Tang, D.F. Liu, S.D. Zhang, W.F. Huang, Mechanical properties and flame-retardant of PP/MRP/$Mg(OH)_2$/$Al(OH)_3$ composites, Compos. Part B Eng. 71 (2015) 74–81.

[37] N. Ranjbar, M. Zhang, Fiber-reinforced geopolymer composites : A review, Cem. Concr. Compos. 107 (2020) 103498.

[38] C. Shi, Z. Wu, J. Xiao, D. Wang, Z. Huang, Z. Fang, A review on ultra high performance concrete: Part I. Raw materials and mixture design, Constr. Build. Mater. 101 (2015) 741–751.

[39] N. Toropovs, F. Lo Monte, M. Wyrzykowski, B. Weber, G. Sahmenko, P. Vontobel, R. Felicetti, P. Lura, Real-time measurements of temperature, pressure and moisture profiles in High-Performance Concrete exposed to high temperatures during neutron radiography imaging, Cem. Concr. Res. 68 (2015) 166–173.

[40] ISO 834-1, Fire resistance tests-elements of building construction-Part 1: general requirements, Geneva, (1999).

[41] ASTM D7309, Standard test method for determining flammability characteristics of plastics and other solid materials, West Conshohocken, (2007).

[42] Y. Zhang, J.W. Ju, Q. Chen, Z. Yan, H. Zhu, Characterizing and analyzing the residual interfacial behavior of steel fibers embedded into cement-based matrices after exposure to high temperatures, Compos. Part B. 191 (2020) 107933.

[43] GB/T 50081, Chinese code for test methods of concrete physical and mechanical properties, Beijing, (2019).

[44] T. Zhang, Y. Zhang, H. Zhu, Z. Yan, Characterizing the thermal properties of hybrid polypropylene-steel fiber reinforced concrete under heat exposure: Insights into fiber geometry and orientation distribution, Compos. Struct. 275 (2021) 114457.

[45] V.K.R. Kodur, S. Banerji, R. Solhmirzaei, Test methods for characterizing concrete properties at elevated temperature, Fire Mater. (2019) 1–15.

[46] T. Zhang, Y. Zhang, H. Zhu, Z. Yan, Experimental investigation and multi-level modeling of the effective thermal conductivity of hybrid micro-fiber reinforced cementitious composites at

elevated temperatures, Compos. Struct. 256 (2021) 112988.
[47] ISO 22007-2, Plastics-Determination of thermal conductivity and thermal diffusivity, Geneva, (2015).
[48] W. Wilson, K.J. Krakowiak, F.J. Ulm, Simultaneous assessment of phase chemistry, phase abundance and bulk chemistry with statistical electron probe micro-analyses: Application to cement clinkers, Cem. Concr. Res. 55 (2014) 35–48.
[49] Q. Zeng, K. Li, T. Fen-chong, P. Dangla, Pore structure characterization of cement pastes blended with high-volume fly-ash, Cem. Concr. Res. 42 (2012) 194–204.
[50] G. Fang, M. Zhang, Multiscale micromechanical analysis of alkali-activated fly ash-slag paste, Cem. Concr. Res. 135 (2020) 106141.
[51] M.K. Seo, J.R. Lee, S.J. Park, Crystallization kinetics and interfacial behaviors of polypropylene composites reinforced with multi-walled carbon nanotubes, Mater. Sci. Eng. A. 404 (2005) 79–84.
[52] Z. Wang, P. Lv, Y. Hu, K. Hu, Thermal degradation study of intumescent flame retardants by TG and FTIR: Melamine phosphate and its mixture with pentaerythritol, J. Anal. Appl. Pyrolysis. 86 (2009) 207–214.
[53] W. Chen, L. Wang, G. Liu, Synthesis of ammonium polyphosphate with crystalline form v (APP-V) from melamine polyphosphate (MPP), Polym. Degrad. Stab. 97 (2012) 2567–2570.
[54] S. Zhang, A.R. Horrocks, A review of flame retardant polypropylene fibres, Prog. Polym. Sci. 28 (2003) 1517–1538.
[55] G. Wang, Y. Wang, J. Yang, Influences of polymerization degree of ammonium polyphosphate on fire protection of waterborne intumescent fire resistive coating, Surf. Coatings Technol. 206 (2012) 2275–2280.
[56] Z. Wang, E. Han, W. Ke, Influence of nano-LDHs on char formation and fire-resistant properties of flame-retardant coating, Prog. Org. Coatings. 53 (2005) 29–37.
[57] X. Ye, Y. Wang, Z. Zhao, H. Yan, A novel hyperbranched poly(phosphorodiamidate) with high expansion degree and carbonization efficiency used for improving flame retardancy of APP/PP composites, Polym. Degrad. Stab. 142 (2017) 29–41.
[58] Z. Wang, E. Han, W. Ke, Effect of nanoparticles on the improvement in fire-resistant and anti-ageing properties of flame-retardant coating, Surf. Coatings Technol. 200 (2006) 5706–5716.
[59] H. Chen, T. Wang, Y. Wen, X. Wen, D. Gao, R. Yu, X. Chen, E. Mijowska, T. Tang, Expanded graphite assistant construction of gradient-structured char layer in PBS/$Mg(OH)_2$ composites for improving flame retardancy, thermal stability and mechanical properties, Compos. Part B Eng. 177 (2019) 107402.
[60] Y. Xia, F. Jin, Z. Mao, Y. Guan, A. Zheng, Effects of ammonium polyphosphate to pentaerythritol ratio on composition and properties of carbonaceous foam deriving from intumescent flame-retardant polypropylene, Polym. Degrad. Stab. 107 (2014) 64–73.
[61] M. Chen, Z. Sun, W. Tu, X. Yan, M. Zhang, Behaviour of recycled tyre polymer fibre reinforced concrete at elevated temperatures, Cem. Concr. Compos. 124 (2021) 104257.

[62] W. Zheng, H. Li, Y. Wang, Compressive behaviour of hybrid fiber-reinforced reactive powder concrete after high temperature, Mater. Des. 41 (2012) 403–409.
[63] S. Sanchayan, S.J. Foster, High temperature behaviour of hybrid steel–PVA fibre reinforced reactive powder concrete, Mater. Struct. 49 (2016) 769–782.
[64] Q.H. Li, C.J. Sun, S.L. Xu, Thermal and mechanical properties of ultrahigh toughness cementitious composite with hybrid PVA and steel fibers at elevated temperatures, Compos. Part B Eng. 176 (2019) 107201.
[65] F. Deng, L. Xu, Y. Chi, F. Wu, Q. Chen, Effect of steel-polypropylene hybrid fiber and coarse aggregate inclusion on the stress–strain behavior of ultra-high performance concrete under uniaxial compression, Compos. Struct. 252 (2020) 112685.
[66] W. Zheng, B. Luo, Y. Wang, Stress–strain relationship of steel-fibre reinforced reactive powder concrete at elevated temperatures, Mater. Struct. 48 (2015) 2299–2314.
[67] A.H. Akca, N.Ö. Zihnioğlu, High performance concrete under elevated temperatures, Constr. Build. Mater. 44 (2013) 317–328.
[68] M. Ozawa, S. Subedi Parajuli, Y. Uchida, B. Zhou, Preventive effects of polypropylene and jute fibers on spalling of UHPC at high temperatures in combination with waste porous ceramic fine aggregate as an internal curing material, Constr. Build. Mater. 206 (2019) 219–225.
[69] EN 1992-1-2, Design of concrete structures, Part 1-2: general rules of structural fire design, Brussels, (2004).
[70] ACI/TMS 216.1, Code requirements for determining fire resistance of concrete and masonry construction assemblies, Farmington Hills, (2014).
[71] F. Wu, L. Xu, Y. Chi, Y. Zeng, F. Deng, Q. Chen, Compressive and flexural properties of ultra-high performance fiber-reinforced cementitious composite: The effect of coarse aggregate, Compos. Struct. 236 (2020) 111810.
[72] M. Abid, X. Hou, W. Zheng, R.R. Hussain, High temperature and residual properties of reactive powder concrete–A review, Constr. Build. Mater. 147 (2017) 339–351.
[73] GB 50016-2014, Chinese code for fire protection design of buildings, Beijing, (2018).
[74] J.Z. Liang, Thermal conductivity of PP/Al(OH)3/Mg(OH)2 composites, Compos. Part B Eng. 44 (2013) 248–252.
[75] W. Zheng, B. Luo, Y. Wang, Microstructure and mechanical properties of RPC containing PP fibres at elevated temperatures, Mag. Concr. Res. 66 (2014) 397–408.
[76] V.K.R. Kodur, M.A. Sultan, Effect of temperature on thermal properties of high-strength concrete, J. Mater. Civ. Eng. 15 (2003) 101–107.
[77] W. Khaliq, V. Kodur, Thermal and mechanical properties of fiber reinforced high performance self-consolidating concrete at elevated temperatures, Cem. Concr. Res. 41 (2011) 1112–1122.
[78] M. Javad, A. Qomi, F. Ulm, R.J. Pellenq, Physical origins of thermal properties of cement paste, Phys. Rev. Appl. 3 (2015) 064010.
[79] S. Xu, J. Liu, Q. Zeng, Towards better characterizing thermal conductivity of cement-based

materials: The effects of interfacial thermal resistance and inclusion size, Mater. Des. 157 (2018) 105–118.

[80] W. Zhang, H. Min, X. Gu, Y. Xi, Y. Xing, Mesoscale model for thermal conductivity of concrete, Constr. Build. Mater. 98 (2015) 8–16.

[81] J. Wang, J. Tao, L. Li, C. Zhou, Q. Zeng, Thinner fillers, coarser pores? A comparative study of the pore structure alterations of cement composites by graphene oxides and graphene nanoplatelets, Compos. Part A Appl. Sci. Manuf. 130 (2020) 105750.

[82] D. Li, D. Niu, Q. Fu, D. Luo, Fractal characteristics of pore structure of hybrid Basalt-Polypropylene fibre-reinforced concrete, Cem. Concr. Compos. 109 (2020) 103555.

[83] L. Sorelli, G. Constantinides, F.J. Ulm, F. Toutlemonde, The nano-mechanical signature of Ultra High Performance Concrete by statistical nanoindentation techniques, Cem. Concr. Res. 38 (2008) 1447–1456.

[84] A.J. Allen, J.J. Thomas, H.M. Jennings, Composition and density of nanoscale calcium-silicate-hydrate in cement, Nat. Mater. 6 (2007) 311–316.

[85] Y. Zhang, J.W. Ju, H. Zhu, Z. Yan, A novel multi-scale model for predicting the thermal damage of hybrid fiber-reinforced concrete, Int. J. Damage Mech. 29 (2019) 19–44.

[86] Q. Chen, H. Zhu, Z. Yan, J.W. Ju, Z. Jiang, Y. Wang, A multiphase micromechanical model for hybrid fiber reinforced concrete considering the aggregate and ITZ effects, Constr. Build. Mater. 114 (2016) 839–850.

[87] M. Chen, W. Chen, H. Zhong, D. Chi, Y. Wang, M. Zhang, Experimental study on dynamic compressive behaviour of recycled tyre polymer fibre reinforced concrete, Cem. Concr. Compos. 98 (2019) 95-112.

[88] M. Chen, H. Zhong, H. Wang, M. Zhang, Behaviour of recycled tyre polymer fibre reinforced concrete under dynamic splitting tension, Cem. Concr. Compos. 114 (2020) 103764.

[89] Y. Wang, H. Zhong, M. Zhang, Experimental study on static and dynamic properties of fly ash-slag based strain hardening geopolymer composites, Cem. Concr. Compos. 129 (2022) 104481.